Geochemistry, Geophysics, Geosystems®

AGU ADVANCING EARTH AND SPACE SCIENCES

RESEARCH ARTICLE
10.1029/2023GC010968

Key Points:

- Serpentinization and rodingitization in the subduction channel as well as carbonation in mud volcano conduits were identified
- Overall evolution of the slab-derived fluid was narrowed down to temperatures from c. 350° to c. 100°C and below
- Serpentinization degree increases with proximity to the trench

Supporting Information:

Supporting Information may be found in the online version of this article.

Correspondence to:

I. Miladinova,
irena.miladinova@uni-graz.at

Citation:

Miladinova, I., Kurz, W., & Hilmbauer-Hofmarcher, T. (2023). Fluid-mantle interaction along the Mariana convergent margin. *Geochemistry, Geophysics, Geosystems*, *24*, e2023GC010968. https://doi.org/10.1029/2023GC010968

Received 24 MAR 2023
Accepted 23 JUL 2023

Fluid-Mantle Interaction Along the Mariana Convergent Margin

Irena Miladinova[1], Walter Kurz[1], and Thomas Hilmbauer-Hofmarcher[1]

[1]Institute of Earth Sciences, NAWI Graz Geocenter, University of Graz, Graz, Austria

Abstract Active serpentinite mud volcanoes in the forearc region of the Izu-Bonin-Mariana system represent an excellent natural laboratory for studying the geochemical processes along convergent plate margins and the associated forearc. During IODP Expedition 366, serpentinite mud with lithic clasts from the underlying forearc crust and mantle as well as from the subducting Pacific Plate was recovered. Ultramafic clasts from Fantangisña Seamount reveal very high degrees of serpentinization with mesh and bastite textures as well as development of late lizardite and chrysotile veins, which suggests serpentinization temperatures below 200°C. On the other hand, recovered harzburgites and, on occasion, dunites from Asùt Tesoru Seamount show a well-preserved primary assemblage with low degrees of serpentinization and forearc peridotite characteristics. Fine-grained antigorite associating with lizardite has been identified throughout the serpentine mud matrix, suggesting an alteration temperature of c. 340°C. Furthermore, alteration conditions during rodingitization point to temperatures of at least 228°C, estimated via chlorite geothermometry. Additionally, a rare ophicarbonate clast containing andraditic as well as Cr-rich hydrogarnets from Asút Tesoru Seamount indicates crystallization temperatures of at least 230°C. Hence, a trend of lower temperature of serpentinization and higher degree of alteration closer to the trench. The detailed characterization of the fluid-rock alteration conditions as well as fluids composition and transport permits a better constraining of the fluid–rock interactions and related mass transfers within subduction zones and during ascent of serpentinite fault gouge within mud volcano conduits and in mudflows after their emplacement on the flanks of the edifices.

Plain Language Summary The fluid migration and circulation in subduction zones play a crucial role in the geochemical cycling as well as the physical and mechanical processes taking place there. Characterizing their nature, source and pathways would contribute to a better understanding not only of the rheology and fluid recycling but also of the tectonic and metamorphic processes operating deep within the Earth's lithosphere as a whole. During an International Ocean Discovery Program (IODP) Expedition, 366 serpentinite mud volcanoes located on the fractured forearc of the Mariana subduction system were drilled. The recovered material consists of highly hydrated rocks that experienced varying degrees of metamorphism and alteration. Mineralogical and chemical composition study of these rocks showed that they are former mantle rocks formed by the infiltration of fluids within the subduction zone. Some of them experienced additional transformation during their ascent to the seafloor by acquiring substantial amount of CO_2-rich minerals. Furthermore, the results show a trend in which alteration temperature is decreasing but transformation degree is increasing with proximity to the subduction channel.

1. Introduction

Geologic processes at convergent plate margins control seismicity, geochemical cycling, and deep biosphere activity in subduction zones. Two approaches are typically taken to study such zones. One approach is to characterize inputs into a convergent plate margin by sampling the down-going plate (e.g., Chan & Kastner, 2000), providing the geochemical reference necessary to elucidate what geochemical factors may influence the production of supra-subduction zone (SSZ) crust and mantle (e.g., Reagan et al., 2017). A second approach is to study outputs in terms of magma and volatiles in volcanic arcs and back-arc basin settings (e.g., Kelemen & Manning, 2015). Such outputs constrain processes that exist deep within the subduction zone and the lithosphere in its hanging-wall. However, neither approach is able to constrain processes that occur within the large and dynamic zone that exists between the site where the subducting plate enters the trench and the location where it reaches the zone of magma genesis beneath the volcanic arc.

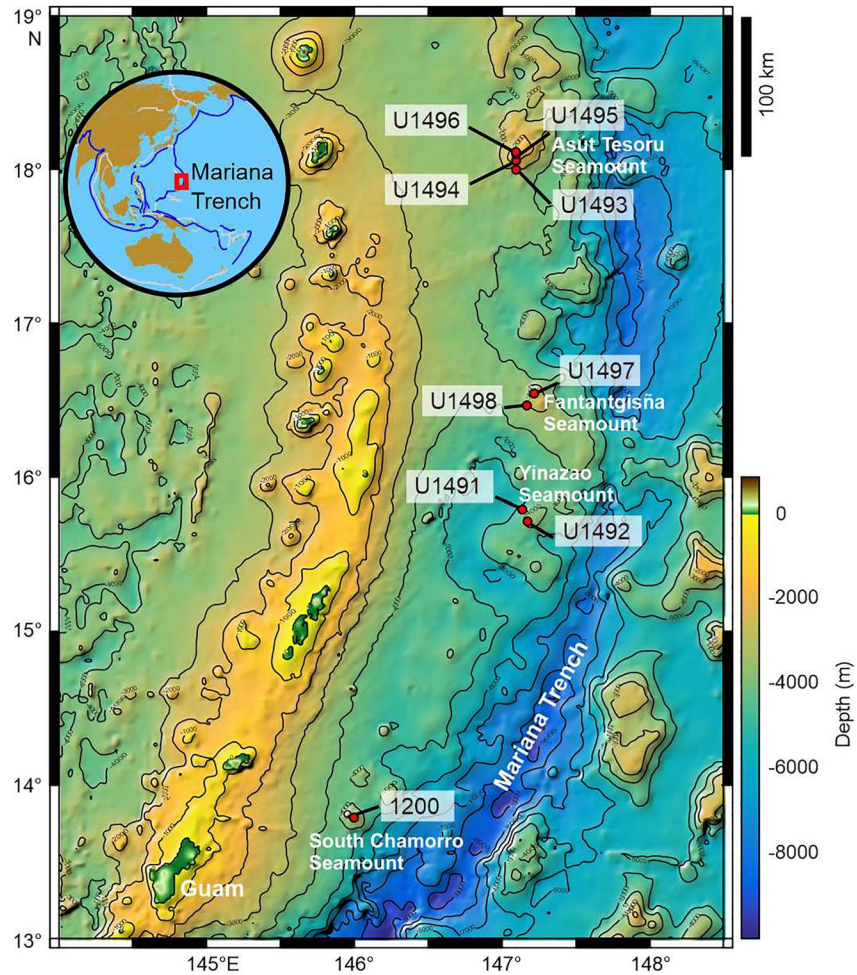

Figure 1. Topographic bathymetric map of the Mariana forearc region showing the drilling locations for IODP Expedition 366 (modified after Fryer et al., 2018).

Determining unequivocally the composition of slab-derived fluids and their influences over the physical properties of the subduction zone or geochemical cycling in convergent margins requires direct sampling of the plate boundary, more specifically the subduction channel. Most studies of subduction channel materials, mass fluxes and geochemical interchanges have been based on data from samples of drill cores, borehole observatories and mud volcanoes in accretionary convergent margins, as well as models based on geophysical considerations (e.g., Fryer et al., 2018; Hensen et al., 2004; Kastner et al., 1993; Peacock et al., 2005; Saffer & Tobin, 2011; Solomon et al., 2009; Tryon et al., 2010). However, large wedges of accreted sediment bury the underlying crystalline basement, making it inaccessible by drilling, and the wedges interact with slab-derived fluids by altering the chemical composition of the slab-derived fluids. Thus, dehydration reactions and metamorphic interchanges in the intermediate and deeper parts of the subduction channel have yet to be sampled in these margins. In contrast, non-accretionary convergent margins can provide a more pristine slab-fluid signature because there is no thick accretionary sediment wedge for the fluids to interact with, and fluid and material egress occurs through fault zones that have experienced water-rock interactions for millions of years, thus minimizing exchange during ascent (Fryer, 1996).

The Mariana convergent margin provides the environment where a natural process brings materials from great depths directly to the surface (e.g., Fryer, 2012). Here, active serpentinite mud volcanoes provide a window to the subduction channel between the subducting Pacific Plate and the Philippine Sea Plate (Figure 1; Fryer & Fryer, 1987; Wheat et al., 2008). The Mariana subduction system is non-accretionary and the forearc is pervasively faulted (Fryer, 1992). Here, serpentinite mud volcanoes are numerous, large (averaging 30 km diameter

and 2 km high) and active (Fryer, 1992, 1996; Fryer & Fryer, 1987). They are composed principally of unconsolidated flows of serpentine muds containing clasts of serpentinized mantle peridotite and several other lithologies, such as blueschist materials derived from the subducting slab (e.g., Fryer, 2012; Maekawa et al., 1995; Pabst et al., 2011) via deep-seated faults.

The Mariana forearc contains the only currently active serpentine mud volcanism in a convergent margin setting. Hence, these mud volcanoes are currently the most direct route to a subduction channel on Earth and because they exist at a range of distances from the trench, they provide a window that allows us to document processes and conditions at depths up to 18 km beneath the forearc (Hulme et al., 2010; Oakley et al., 2007). Fluids upwell within these mud volcanoes at a rate that is in excess of the mud matrix (Fryer et al., 1999; Hulme et al., 2010). Such fluids originate from the down-going plate but are highly altered, are reducing and have pH values in the range of 9–12.5 (Hulme et al., 2010; Mottl et al., 2003, 2004; Wheat et al., 2008).

IODP Expedition 366 recovered cores from three serpentinite mud volcanoes at increasing distances from the Mariana Trench: Yinazao (Blue Moon), Fantangisña (Celestial), and Asùt Tesoru (Big Blue) (Figure 1; Fryer et al., 2018). The recovered material consists of highly indurated serpentinite mud with embedded lithic clasts of mainly peridotitic rocks and minor amounts of mafic rocks, all of which have experienced varying degrees of metamorphism and/or alteration. Their mineralogical and chemical compositions show that they are formed by the infiltration of fluids within the subduction zone. For the purposes of this study, we investigated the textural and mineral chemical evolution of ultramafic and mafic rock clasts from the flanks and summits of both Asùt Tesoru and Fantangisña Seamounts. We also analyzed several samples of serpentine mud from Asùt Tesoru Seamount that commonly contain varying amounts of fine-grained lithic clasts (>2 mm) (Table 1). Our detailed examination of serpentinization and rodingitization processes as well as carbonation of serpentinites permits reconstruction of the mechanisms of forearc mantle alteration, fluid activity and fluid-rock interaction.

2. Geological Overview

The Izu-Bonin-Mariana (IBM) convergent margin in the western Pacific Ocean is a non-accretionary, intra-oceanic arc system that formed during the subduction of the Pacific Plate under the Philippine Sea plate since Eocene times (e.g., Fryer, 1996; Ishizuka et al., 2018; Kurz et al., 2019; Reagan et al., 2019; Stern et al., 2003). Within the southern IBM segment (Mariana), the convergent margin exhibits a sequential formation of volcanic arcs and extensional back-arc basins (e.g., Fryer, 1996; Hussong & Uyeda, 1982; Reagan et al., 2019; Stern & Bloomer, 1992; Stern et al., 2003; Taylor & Fujioka, 1992) including the Mariana Trough and forearc at the eastern edge of the Philippine Sea Plate. Furthermore, the forearc is pervasively faulted due to across- and along-strike extension as well as vertical tectonic deformation that is related to the subduction of seamounts (Figure 1; Fryer & Fryer, 1987; Fryer & Pearce, 1992; Fryer & Salisbury, 2006; Kurz et al., 2019). These fault systems allow the rising and exhumation of serpentinite gouge that is mobilized by slab-derived fluids from the forearc lithospheric mantle, forming km-scale serpentine mud seamounts (e.g., Fryer, 2012).

Active serpentinite mud volcanoes are currently restricted only to the IBM forearc; within the Mariana forearc they occur up to a distance of 100 km away from the trench. The seamount-trench distance basically correlates with a range of depth and temperature of the down-going plate and the subduction channel (Figure 1; Fryer, 2012; Fryer et al., 1999, 2000, 2006). The positions of the serpentinite mud volcanoes are related to active seeps, which penetrate the forearc lithosphere and can reach depths up to 18 km, providing direct access to the subduction channel as well as monitoring of different metamorphic and metasomatic processes operating as the Pacific Plate lithosphere subducts (e.g., Fryer et al., 2020). A decrease in the degree of serpentinization of the mantle wedge beneath the forearc may limit the distance of the serpentinite seamounts from the subduction front (Fryer et al., 2000; Stern & Smoot, 1998). This assumption is supported by formerly drilled cores with only slightly altered ultramafic samples (ODP Leg 125), suggesting that the sub-forearc mantle is not entirely serpentinized (Fryer et al., 2000; Oakley et al., 2007). However, according to other studies, the forearc mantle wedge displays a much higher degree of serpentinization of at least 50% (Bostock et al., 2002; Nagaya et al., 2016).

The mud volcanoes are composed of unconsolidated clay-to silt-sized serpentinite mud containing up to boulder-sized clasts of variably serpentinized mantle peridotites as well as crustal and subducted Pacific Plate materials, including blueschist-facies clasts (e.g., Fryer, 2012; Maekawa et al., 1995; Pabst et al., 2011; Tamblyn et al., 2019). The deep-sourced formation fluids originate from the dehydration of the down-going slab, whereby c. 30%–70% of the subducted formation water is released beneath the forearc mantle and just 15%–35% of the

Table 1
List of the Investigated Samples Including IODP Sample Code

Sample	Seamount	Sample code IODP	Depth (mbsf)	Lithology
1-1493B-56	Asùt Tesoru	366-U1493B-2X-1-W 19/21	0.89	Oxidized sandy mud with carbonate
1-1493B-57	Asùt Tesoru	366-U1493B-2X-1-W 29/32	0.99	Ophicarbonate
1-1493B-61*	Asùt Tesoru	366-U1493B-3F-5-W 50/60	14.63	Blue serpentinite mud
1-1493B-62	Asùt Tesoru	366-U1493B-4F-CC-W 20/30	18.88	Blue serpentinite mud
1-1493B-63*	Asùt Tesoru	366-U1493B-6F-3-W 25/40	26.66	Green serpentinite mud
1-1493B-64	Asùt Tesoru	366-U1493B-8F-CC-W 34/44	29.54	Green serpentinite mud
1-1493B-68	Asùt Tesoru	366-U1493B-9X-1-W 71/74	30.31	Harzburgite, serpentinized
1-1494A-73	Asùt Tesoru	366-U1494A-1F-4-W 33/36	3.44	Blue to green serpentine mud
1-1494A-74	Asùt Tesoru	366-U1494A-1F-CC-W 5/15	4.23	Blue to green serpentine mud with foraminifera
1-1494A-78	Asùt Tesoru	366-U1494A-3F-4-W 50/60	12.68	Blue to green serpentine mud
1-1494A-79*	Asùt Tesoru	366-U1494A-5F-2-W 5/23	19.41	Blue serpentinite mud
1-1494A-80	Asùt Tesoru	366-U1494A-5F-2-W 71/85	20.07	Blue serpentinite mud
1-1494A-81*	Asùt Tesoru	366-U1494A-5F-3-W 98/113	21.30	Blue serpentinite mud
1-1494A-82	Asùt Tesoru	366-U1494A-6F-2-W 15/23	24.00	Blue serpentinite mud
1-1494A-83	Asùt Tesoru	366-U1494A-9G-1-W 30/40	31.33	Blue serpentinite mud
1-1494A-84	Asùt Tesoru	366-U1494A-10F-1-W 32/38	32.92	Blue serpentinite mud
1-1494A-85	Asùt Tesoru	366-U1494A-10F-2-W 46/56	33.85	Blue serpentinite mud
1-1494A-86	Asùt Tesoru	366-U1494A-10F-2-W 100/106	34.39	Blue serpentinite mud
1-1495B-89*	Asùt Tesoru	366-U1495B-2F-CC-W 15/25	4.20	Blue serpentinite mud
1-1495B-95*	Asùt Tesoru	366-U1495B-4F-3-W 70/80	8.80	Blue serpentinite mud
1-1496A-270	Asùt Tesoru	366-U1496A-2F-2-W 38/49	4.83	Blue serpentinite mud
1-1496A-100	Asùt Tesoru	366-U1496A-3F-5-W 46/48	11.89	Dunite, serpentinized
TSB-73	Asùt Tesoru	366-U1496A-3F-5-W 96/98	12.39	Reaction zone (grt + chl)
1-1496A-102	Asùt Tesoru	366-U1496A-3F-CC-W 17/19	12.67	Rodingite
1-1496A-103*	Asùt Tesoru	366-U1496A-4F-4-W 18/28	16.45	Blue serpentinite mud
1-1496A-105	Asùt Tesoru	366-U1496A-5F-3-W 83/93	20.79	Blue serpentinite mud
1-1496A-106	Asùt Tesoru	366-U1496A-6F-2-W 47/51	22.80	Harzburgite, serpentinized
1-1496A-110	Asùt Tesoru	366-U1496A-6F-5-W 60/70	26.43	Blue serpentinite mud
1-1496A-113	Asùt Tesoru	366-U1496A-8F-2-W 41/51	33.01	Blue serpentinite mud
1-1496B-118	Asùt Tesoru	366-U1496B-3F-2-W 30/40	7.29	Blue serpentinite mud
1-1496B-123	Asùt Tesoru	366-U1496B-5F-1-W 85/95	16.85	Blue serpentinite mud
1-1496B-125	Asùt Tesoru	366-U1496B-6F-2-W 0/6	22.22	Blue serpentinite mud
1-1496B-126	Asùt Tesoru	366-U1496B-6F-2-W 41/51	22.63	Blue serpentinite mud
1-1496C-135	Asùt Tesoru	366-U1496C-5R-1-W 8/10	36.68	Harzburgite, serpentinized
1-1496C-136	Asùt Tesoru	366-U1496C-7R-1-W 0/2	55.60	Harzburgite, serpentinized
1-1496C-138	Asùt Tesoru	366-U1496C-11R-1-W 30/33	94.20	Harzburgite, serpentinized
1-1496C-139	Asùt Tesoru	366-U1496C-11R-3-W 40/43	96.64	Harzburgite, serpentinized
1-1498B-210	Fantangisna	366-U1498B-3R-3-W 89/92	21.29	Harzburgite, serpentinized
1-1498B-211	Fantangisna	366-U1498B-4R-1-W 90/94	29.80	Harzburgite, serpentinized
1-1498B-212	Fantangisna	366-U1498B-4R-2-W 30/32	30.32	Harzburgite, serpentinized
1-1498B-214	Fantangisna	366-U1498B-5R-1-W 56/59	35.26	Harzburgite, serpentinized
1-1498B-224	Fantangisna	366-U1498B-7R-4-W 79/82	57.38	Harzburgite, serpentinized

Table 1
Continued

Sample	Seamount	Sample code IODP	Depth (mbsf)	Lithology
1-1498B-237	Fantangisna	366-U1498B-13R-1-W 33/36	112.83	Harzburgite, serpentinized
1-1498B-249	Fantangisna	366-U1498B-20R-1-W 27/34	180.87	Harzburgite, serpentinized

Note. Samples with (*) were selected for XRF analysis.

fluid derived from the subducted plate is released beneath volcanic fronts causing arc magmatism (e.g., Fryer et al., 2020; Hyndman & Peacock, 2003; Mottl, 1992; Peacock, 1990; Rupke et al., 2004; Schmidt & Poli, 1998).

Several studies confirmed the episodicity of serpentinite mudflows formation from a central conduit due to the presence of multiple mudflow units on the flanks of the seamounts (Frery et al., 2021; Fryer, 1992; Fryer et al., 1990; Oakley et al., 2007; Wheat et al., 2008). The presence of clay layers within the serpentinite mud flow deposits may represent quiet phases between serpentinite mud eruptions (Fryer, 1996). The oldest indications for serpentinization processes within the arc system were found in sediments of middle Eocene age (Fryer et al., 2006). Based on biostratigraphic data the latest recorded phase of serpentinite mud volcano activity is Late Miocene to Early Pliocene (c. 6–4 Ma; Del Gaudio et al., 2022). In a plate tectonic context, these data are corresponding to the initiation of spreading within the Mariana Trough at 6–7 Ma and with true seafloor spreading initiating at 3–4 Ma, forming the remnant arc of the West Mariana Ridge (e.g., Anderson et al., 2017; Clift & Lee, 1998; Oakley et al., 2009; Sato et al., 2015; Stern et al., 2003; Straub et al., 2010).

2.1. Drilling Sites Description

International Ocean Discovery Program (IODP) Expedition 366 recovered cores from three serpentinite mud volcanoes at increasing distances from the Mariana Trench (Yinazao, Fantangisña and Asùt Tesoru), which are located at 55, 62 and 72 km from the trench axis, respectively (Figure 1; Fryer et al., 2018). The drilling sites were located on the summit regions, which represent active sites of eruption, but also on the flanks of the mud volcanoes, where ancient flows are overlain by more recent ones. The recovery includes pelagic sediments, volcanic rocks (boninites and forearc basalts) and peridotite clasts from the forearc mantle wedge. Recycled materials from the subducted slab are found at all three mud volcanoes and consist of metavolcanic rocks (metamorphosed tholeiitic and alkali basalts), metamorphosed pelagic sediments including cherty limestone as well as fault rocks with various degrees of deformation.

Fantangisña Seamount (informally known as Celestial Seamount) is located at 16°32′N, 147°13′E, about 62 km from the trench and about 14 km above the subducting Pacific Plate (Fryer et al., 2018; Oakley, 2008). This edifice lies on the northern edge of an uplifted forearc block that trends NW. Side-scan backscatter of the seamount shows several deep erosional channels on the western flanks as well as a prominent slump on the northern flank. At the base of the western flank of the seamount, numerous large blocks, as wide as 2 km, are possibly the result of slumps that brought down large portions of the seamount (Oakley et al., 2007).

Site U1497 is located in the center of a depression at the summit of Fantangisña Seamount (Figure 1). The serpentinite mud deposits here appear to be consolidated and viscous and exhibit reddish oxidized zones, which underlie the uppermost intervals of dark bluish gray muds, suggesting significant episodes of oxidation during exposure at the seafloor. The ultramafic lithic clasts within the muds are generally highly serpentinized, consistent with a long residence time in high-pH fluids. However, they may retain evidence of primary textures including pseudomorphs after orthopyroxene as well as primary spinel, indicating deformation at relatively low temperatures and moderate to high strain rates. The metasedimentary and volcanic rocks are characterized by various degrees of brecciation with development of fine-grained cataclasite to ultracataclasite domains, suggesting low-grade deformation mechanisms and/or comparably high strain rates. Together with the presence of Ti-bearing augite, which indicates an ocean island basalt alkali provenance, this suggests that a significant fraction of the material entrained by this mud volcano was derived from the subducting Pacific Plate (Fryer et al., 2018).

Site U1498 was drilled on the southwestern flank (Figure 1) and consists of a wide variety of materials, including serpentinite sands and silts, oxidized muds with pelagic microfossils, partially serpentinized ultramafic rocks (harzburgite and dunite), mafic metavolcanic rocks as well as nannofossil- and volcanic ash–rich sedimentary rocks (siltstones and fine sandstones). Additionally, within core 366-U1498B-21R, metabasite overlies cherty

limestone and the preserved primary contact between them is inverted. The texture and mineralogical composition of both lithologies indicates low-to medium-grade metamorphic overprint. Preserved cataclastic faults and extensional structures might be related either to shearing within the subduction channel and bending of the lower plate during subduction or to faulting during the early stages of exhumation. Hence, the mafic metavolcanic-carbonate interval is considered to represent a remnant of a subducted guyot from the Pacific Plate (Fryer et al., 2018). The lowermost cored intervals in Holes U1498A and U1498B are deposits of microfossil-bearing volcanic ash defining the seafloor upon which the mud volcano was built.

Asùt Tesoru Seamount (informally called Big Blue Seamount) is located north of Fantangisña, at approximately 18°06′N and 147°06′E. The serpentinite mud volcano is about 72 km from the trench axis and approximately 18 km above the subducting slab (Oakley et al., 2007, 2008). It is the farthest from the trench of the three drilled seamounts and also the largest one on the Mariana forearc, with a diameter of ∼50 km and over 2 km high.

Sites U1493, U1494 and U1495 were drilled on the southern flank of the Asùt Tesoru Seamount (Figure 1). All three sites show a common stratigraphy that differs in detail upslope. The deepest site, U1493, has a thick layer of reddish oxidized sediments immediately below the seafloor that includes microfossiliferous pelagic muds overlying serpentinite muds. Sites farther up the flank have thinner oxidized zones, thinner pelagic sediment and fewer microfossils. Carbonated ultramafic breccias and altered ultramafic clasts are the most common rock types in the shallow serpentinite muds. In the deep parts of the flank sites, massive as well as foliated ultramafic clasts (harzburgite and dunite with rare pyroxenite) exhibiting various degrees of serpentinization were recovered. Low-grade mafic metavolcanic rocks show compositional characteristics either of shallow subducted oceanic crust or of the forearc crust beneath the mud volcano (Fryer et al., 2018).

Site U1496 is located at the summit of the Asùt Tesoru Seamount (Figure 1). The recovered materials consist of minor pelagic sediment overlying serpentinite muds that are underlain by moderately to highly consolidated serpentinite sequences within the active eruptive region of this serpentinite mud volcano. Generally, the proportion of lithic clasts compared to the flanks and other sites is low. The serpentinite muds recovered in the cores are very soft due to their high water and gas content, which is typical for active summits currently producing high-pH interstitial water and abiotic hydrogen and methane (Fryer et al., 2018). The recovered hard rock clasts are mainly ultramafics, typically serpentinized harzburgites and rarely dunites and pyroxenites. They are derived from the underlying forearc mantle lithosphere deep within the serpentinite mud volcano's conduit system. Also, present are mafic metavolcanic and sedimentary clasts, including dolerite and fossiliferous cherty limestone. The presence of Ti-rich pyroxene, which indicates an alkali basalt protolith, and Na-rich amphiboles in the metavolcanics suggest that these clasts may be recycled material from the subducted Pacific Plate (Fryer et al., 2018).

3. Analytical Methods

All measurements and analyses were conducted at the Institute of Earth Sciences, NAWI Graz Geocenter, University of Graz.

3.1. Petrographic and Mineralogical Analysis of the Muds

For first estimation of the grain size distribution as well as a semiquantitative identification and characterization of major and minor components within the unlithified fine-grained serpentine mud samples, smear slides were prepared. They were analyzed using an Olympus BX50 petrographic microscope, equipped with a Zeiss Axiocam IC. For training, references and as a guideline for the optical determination of different components, the "IODP Smear Slide Digital Reference for Sediment Analysis of Marine Mud" (Part 1 and 2; Marsaglia et al., 2013, 2015) was used. Furthermore, for the purposes of mineral composition analyses, loose unlithified serpentine mud material was embedded in epoxy resin and polished. Representative pictures of the investigated samples as well as their mineral composition can be found in Supporting Information S1 (Figures S1–S7).

3.2. Bulk Rock and Mineral Composition Analyses

For the whole rock bulk composition analyses, the samples were crushed and representative aliquots of each sample were powdered in an agate mill. Major oxides and trace elements were determined by X-ray fluorescence analysis, carried out using a Bruker Tiger S8-II spectrometer with a Rh target X-ray tube. Loss on ignition (L.O.I.) was determined by weight loss before and after heating every sample up to 1000°C. All the Fe is reported as ferric (Fe^{3+}: Fe_2O_3) in the XRF analysis (Table 2).

Table 2
Whole-Rock Major Oxides (wt%) and Selected Trace Element Contents (ppm) in the Studied Serpentinite Muds From Asùt Tesoru Seamount Obtained by XRF

Sample	1-1493B-61	1-1493B-63	1-1494A-79	1-1494A-81	1-1495B-89	1-1495B-95	1-1496A-103
Major oxides (wt%)							
SiO_2 (%)	41.84	44.89	43.85	43.61	44.15	42.94	43.26
TiO_2 (%)	0.01	0.01	0.01	0.01	0.02	0.02	0.05
Al_2O_3 (%)	0.41	0.54	0.69	0.49	0.63	0.60	0.86
Fe_2O_3 (%)	8.20	7.49	8.39	8.30	7.75	8.00	8.22
MnO (%)	0.06	0.10	0.09	0.09	0.10	0.11	0.12
MgO (%)	47.36	44.50	44.62	45.66	44.72	45.32	44.45
CaO (%)	0.05	0.87	0.48	0.00	0.86	0.71	0.67
K_2O (%)	0.02	0.02	0.02	0.01	0.01	0.02	0.04
Na_2O (%)	0.53	0.37	0.38	0.34	0.26	0.43	0.99
L.O.I.	16.02	13.34	13.82	13.99	13.56	14.01	13.89
Total sum	98.48	98.79	98.53	98.51	98.50	98.15	98.66
Trace elements (ppm)							
Ni	2,492	1,791	2,116	2,661	2,118	2,419	2,405
Cr	2,257	2,111	2,397	2,759	2,420	2,614	2,531
V	23	<20	27	27	28	27	26

For all samples, the major element compositions of minerals as well as the X-ray compositional maps were measured using a JEOL JXA-8530FPlus field emission electron microprobe. Quantitative analyses were performed by using wavelength-dispersive spectrometers (WDS) with 1–10 µm beam diameter with an acceleration voltage of 15 kV and a beam current of 10 nA. Element concentration maps were obtained for Mg, Ca, Fe, Na, Cr and Ti also by WDS using a focused beam with an accelerated voltage of 15 kV and 100 nA beam current. A range of natural standards was used for calibration (Si, Al, Fe: garnet; Mg, Ca: diopside; Na: albite; K: microcline; Mn: rhodonite; Ti: ilmenite; Cr: chromite). Pyroxene-group minerals were classified following the nomenclature of Morimoto et al. (1988); amphibole nomenclature follows Hawthorne et al. (2012) and Oberti et al. (2012). Representative microprobe analyses of minerals from the investigated samples are listed in Table 3.

To identify different carbonate and serpentine varieties as well as brucite, unpolarized Raman spectra were collected in the 150–1,200 cm^{-1} spectral range using a confocal Horiba Jobin Yvon LabRam-HR 800 Raman spectrometer. Samples were excited at room temperature with a 50 mW Nd-YAG laser (532 nm) and a 30 mW He-Ne laser (632.2 nm) through an OLYMPUS 100× objective. The slit width was set to 100 µm. The light was dispersed by a holographic grating with 1,800 grooves/mm and subsequently collected by a 1024 × 256 open electrode charge coupled device (CCD) detector. Calibration and control of the band shifts were done by regularly adjusting the zero position of the grating and measuring the Rayleigh line of the incident laser beam, respectively.

Additionally, X-ray powder diffraction (XRD) was applied for further identification of single mineral phases. The analyzed material was finely ground in an agate mortar and homogenized before being placed on a sample holder in the diffractometer. For determining the average bulk mineralogy of the samples, a Siemens D5000 X-ray diffractometer with a voltage of 40.0 kV and an amperage of 40 mA was used. To perform measurements, a Bragg-Brentano array with fixed sample (2-theta scale) was used, and data were collected from 4.1° to 65° by 0.02° step size with 0.1–0.6 s step time. To identify mineral phases, the resulting diffraction patterns were compared with the Department's computerized database of reference data.

3.3. Chlorite Thermometry

Chlorite is not a common mineral in all investigated rock samples but is well preserved in some. Over the years, various empirical geothermometers have been developed to exploit the relationships between the composition and formation temperature of chlorite (see Bourdelle & Cathelineau, 2015). In this study, we apply the

Table 3
Representative Microprobe Analyses of Minerals in wt% and p.f.u

Seamount	Fantangisna	Fantangisna	Fantangisna	Fantangisna	Fantangisna	Asùt Tesoru	Asùt Tesoru	Asùt Tesoru	Asùt Tesoru	Asùt Tesoru	Asùt Tesoru	Asùt Tesoru
Lithology	SP	SP	SP	SP	SP	SP	SP	SP	SP	SP	SP	SP
Mineral	srp	brc	Cr-spl	chl	grt	ol	opx	di	rit	tr	Cr-spl	srp
SiO_2	44.02	0.79	0.01	34.69	31.58	40.78	58.31	54.47	57.50	57.93	0.01	40.94
TiO_2	0.00	0.00	0.02	1.17	5.53	0.01	0.00	0.01	0.00	0.00	0.00	0.00
Al_2O_3	0.18	0.00	22.65	16.57	0.50	0.00	0.19	1.23	0.08	0.65	19.77	0.21
FeO	3.56	5.09	16.40	15.49	21.64	8.75	5.80	1.78	1.90	1.44	17.23	4.86
MnO	0.03	0.29	0.11	0.13	0.03	0.11	0.14	0.08	0.15	0.02	0.14	0.08
MgO	37.70	66.46	11.36	13.69	0.70	49.96	35.62	18.07	24.07	23.92	11.54	37.30
CaO	0.02	0.02	0.00	0.70	33.45	0.01	0.04	23.49	6.45	12.96	0.01	0.29
Na_2O	0.00	0.00	0.00	2.23	0.02	0.00	0.01	0.14	6.74	0.22	0.00	0.06
K_2O	0.01	0.00	0.00	2.97	0.00	0.02	0.00	0.00	0.35	0.01	0.00	0.03
NiO	0.00	0.00	0.00	0.00	0.00	0.32	0.10	0.07	0.05	0.13	0.00	0.00
Cr_2O_3	0.00	0.00	49.73	0.00	0.13	0.00	0.00	0.45	0.00	0.01	50.85	0.00
Sum	85.52	72.64	100.27	87.64	93.59	99.97	100.20	99.79	97.29	97.27	99.56	83.78
Si	4.18	0.01	0.00	3.50	5.94	1.00	2.00	1.98	7.93	7.91	0.00	4.03
Ti	0.00	0.00	0.00	0.09	0.78	0.00	0.00	0.00	0.00	0.00	0.00	0.00
Al	0.02	0.00	6.58	1.97	0.11	0.00	0.01	0.05	0.01	0.10	5.87	0.02
Fe	0.28	0.08	3.38	1.31	3.41	0.18	0.17	0.05	0.22	0.17	3.63	0.40
Mn	0.00	0.00	0.02	0.01	0.00	0.00	0.00	0.00	0.02	0.00	0.03	0.01
Mg	5.33	1.88	4.17	2.06	0.20	1.82	1.82	0.98	4.95	4.87	4.34	5.47
Ca	0.00	0.00	0.00	0.08	6.74	0.00	0.00	0.91	0.95	1.90	0.00	0.03
Na	0.00	0.00	0.00	0.44	0.01	0.00	0.00	0.01	1.80	0.06	0.00	0.01
K	0.00	0.00	0.00	0.38	0.00	0.00	0.00	0.00	0.06	0.00	0.00	0.00
Ni	0.00	0.00	0.00	0.00	0.00	0.01	0.00	0.00	0.01	0.01	0.00	0.00
Cr	0.00	0.00	9.69	0.00	0.02	0.00	0.00	0.01	0.00	0.00	10.13	0.00
Sum	9.81	1.99	23.86	9.83	17.21	3.00	4.00	4.00	15.94	15.03	24.00	9.97
O	14.00	2.00	32.00	14.00	24.00	4.00	6.00	6.00	22.00	22.00	32.00	14.00
Fo %	-	-	-	-	-	90.96	-	-	-	-	-	-
Cr#	-	-	60.00	-	-	66.69	-	-	-	-	63.31	-
Mg#	91.38	92.89	55.00	-	-	-	-	-	-	-	54.44	88.46
Xadr	-	-	-	-	98.30	-	-	-	-	-	-	-
Xgrs	-	-	-	-	1.20	-	-	-	-	-	-	-
Xuva	-	-	-	-	0.50	-	-	-	-	-	-	-
Xen	-	-	-	-	-	-	91.38	50.21	-	-	-	-

Note. Fe is calculated as Fe^{2+}, except for garnet where Fe is Fe^{3+}. *SP* serpentinized peridotite, *RZ* reaction zone, *OPH* ophicarbonate, *Fo* forsterite, *adr* andradite, *grs* grossular, *uva* uvarovite, *en* enstatite.

Asùt Tesoru	Asùt Tesoru	Asùt Tesoru	Asùt Tesoru	Asùt Tesoru	Asùt Tesoru	Asùt Tesoru	Asùt Tesoru	Asùt Tesoru	Asùt Tesoru	Asùt Tesoru	Asùt Tesoru	Asùt Tesoru
SP	SP	RZ	RZ	RZ	rodingite	rodingite	rodingite	rodingite	OPH	OPH	OPH	OPH
brc	grt	grt	grt, Ti-rich	chl	di	wol	chl	grt	grt	grt, Cr-rich	Cr-spl	srp
11.33	35.23	33.99	30.91	28.77	53.77	53.37	34.40	32.07	34.73	30.48	0.06	42.98
0.00	0.00	3.26	13.40	0.07	0.01	0.21	0.03	6.29	0.37	2.69	0.04	0.00
0.08	0.90	12.62	8.69	14.83	0.28	0.15	12.91	2.12	1.33	0.53	24.93	0.09
10.05	27.16	9.14	5.46	25.69	5.44	9.38	10.59	18.71	26.69	17.13	18.87	0.06
0.14	0.00	0.03	0.10	0.22	0.21	0.70	0.16	0.07	0.04	0.00	0.11	0.06
50.71	0.17	0.13	0.09	17.96	15.04	11.85	28.03	0.84	0.22	0.26	12.91	39.12
0.04	33.33	35.42	34.31	0.56	25.06	24.71	0.64	33.35	33.13	33.58	0.00	0.07
0.02	0.04	0.00	0.09	0.01	0.03	0.09	0.19	0.00	0.00	0.00	0.01	0.00
0.00	0.00	0.00	0.02	0.00	0.01	0.00	0.04	0.00	0.00	0.00	0.00	0.00
0.00	0.00	0.00	0.00	0.00	0.00	0.00	0.00	0.00	0.02	0.01	0.09	0.07
0.00	0.16	0.05	0.00	0.03	0.05	0.03	0.05	0.77	0.00	6.20	42.01	0.00
72.39	96.99	94.65	93.06	88.15	99.89	100.49	87.04	94.24	96.53	90.90	99.04	82.44
0.21	6.46	5.78	5.34	3.03	1.99	2.00	3.36	5.88	6.39	5.90	0.01	4.16
0.00	0.00	0.42	1.74	0.01	0.00	0.01	0.00	0.87	0.05	0.39	0.01	0.00
0.00	0.20	2.53	1.77	1.84	0.01	0.01	1.49	0.46	0.29	0.12	7.27	0.01
0.16	4.16	1.30	0.79	2.26	0.17	0.29	0.86	2.87	4.10	2.77	3.91	0.00
0.00	0.00	0.00	0.01	0.02	0.01	0.02	0.01	0.01	0.01	0.00	0.02	0.00
1.41	0.05	0.03	0.02	2.82	0.83	0.66	4.08	0.23	0.06	0.08	4.77	5.64
0.00	6.54	6.46	6.35	0.06	0.99	0.99	0.07	6.55	6.53	6.96	0.00	0.01
0.00	0.01	0.00	0.03	0.00	0.00	0.01	0.04	0.00	0.00	0.00	0.00	0.00
0.00	0.00	0.00	0.00	0.00	0.00	0.00	0.00	0.00	0.00	0.00	0.00	0.00
0.00	0.00	0.00	0.00	0.00	0.00	0.00	0.00	0.00	0.00	0.00	0.02	0.01
0.00	0.02	0.01	0.00	0.00	0.00	0.00	0.00	0.11	0.00	0.95	8.22	0.00
1.79	17.44	16.53	16.05	10.05	4.00	3.99	9.92	16.97	17.42	17.17	24.23	9.84
2.00	24.00	24.00	24.00	14.00	6.00	6.00	14.00	24.00	24.00	24.00	32.00	14.00
-	-	-	-	-	-	-	-	-	-	-	-	-
-	-	-	-	-	-	-	-	-	-	-	53.06	-
83.46	-	-	-	-	-	-	-	-	-	-	54.96	99.86
-	95.00	42.50	69.60	-	-	-	-	89.30	93.50	76.55	-	-
-	4.50	57.30	30.40	-	-	-	-	8.00	6.50	0.50	-	-
-	0.50	0.20	0.00	-	-	-	-	2.70	0.00	23.00	-	-
-	-	-	-	-	41.52	33.60	-	-	-	-	-	-

geothermometers by Cathelineau (1988), Cathelineau and Nieva (1985) and Jowett (1991) because they are calibrated for low-temperature metamorphic alteration of mafic rocks (e.g., Bevins et al., 1991). All three geothermometers are based on the occupancy of Al(IV) in tetrahedral sites of the chlorite structure as well as the Fe/(Fe + Mg) ratios of chlorite, which correlate positively with the formation temperature of chlorite.

4. Results

4.1. Fantangisña Seamount

Investigated samples from the flank of Fantangisña Seamount (site 1498) contain a wide variety of materials, including ultramafic rocks with various degrees of serpentinization, mafic metavolcanics as well as low-grade metasediments (cherty limestones). The ultramafic rocks show high degrees of serpentinization with well-developed mesh and hourglass as well as bastite textures (Figures 2a–2d). Primary mantle Cr-spinel relicts have been observed. The single crystals are mainly unzoned and homogenous in composition and rarely display a very thin (<5 μm) corona of magnetite. Based on the Cr# (100*Cr/(Cr + Al)) and Mg# (100*Mg/(Mg + Fe^{2+})) values, Cr-spinel can be subdivided into two groups: (a) Cr-spinel showing more elevated Cr# (77–91) and somewhat lower Mg# (21–43), and (b) Cr-spinel with slightly lower Cr# (49–60) but a bit higher Mg# (43–60). The veins are solely composed of chrysotile, whereas the matrix contains chrysotile and lizardite; no antigorite was detected in these samples. In general, serpentine composition is somewhat variable with SiO_2 contents of 30.19–44.02 wt% and MgO of 30.97–44.57 wt%, whereas FeO reaches values up to 9.31 wt% (Table 3). Andraditic garnet occurs throughout the serpentinized matrix mainly in association with bastite (Figure 3a, Table 3). Brucite and magnetite as well as Ni alloys may also be present.

4.2. Asùt Tesoru Seamount

Site U1496 on the summit of Asùt Tesoru Seamount recovered mainly serpentinite mud with less common lithic clasts comprising ultramafic rocks as well as mafic metavolcanics and sedimentary clasts. The finely comminuted matrix of the investigated mud samples is composed of silt-to clay-sized serpentine of pale bluish color. XRD and Raman analyses confirmed the presence of all three serpentine polymorphs, that is, lizardite, chrysotile and antigorite (Figures 4a and 5). The Raman measurements mostly show mixed lizardite-antigorite spectra, suggesting close association of both minerals on micron-scale. Furthermore, larger rock clasts throughout the mud matrix contain chlorite, brucite, magnetite, spinel, relic pyroxene and hydrogarnet as well as fragments of carbonate and rare volcanic glass.

The ultramafic rock clasts display various degrees of serpentinization and often a well-preserved primary assemblage (Figure 6). They are dominantly harzburgite with olivine, orthopyroxene and variable but minor clinopyroxene as well as accessory spinel (Figure 2e). Olivine is unzoned and has forsterite-rich composition with high Mg# (100*Mg/(Mg + Mn + Fe^{2+})) ranging between 90 and 92 (Table 3). Orthopyroxene is Mg-rich with an En component ranging from 88.63% to 91.86%. Clinopyroxene is a rather minor phase and its composition varies between diopside and augite ($En_{48.17\text{-}50.32}Wo_{47.40\text{-}49.46}$; Figure 7a). Spinel is mainly Cr-rich with Cr# of 30–67 and Mg# of 42–76 (Table 3). It is mainly unzoned and rarely shows a very thin corona of magnetite. Garnet with andradite composition is found either within bastite textures or in direct association with clinopyroxene, indicating rather low degrees of serpentinization. Raman spectra identified serpentine in the form of lizardite and chrysotile in the matrix and in veins. Serpentine composition is less variable, with SiO_2 of 37.42–44.10 wt% and MgO between 38.42 and 40.28 wt%. FeO is rather low and reaches up to 4.08 wt% (Table 3). Brucite is also found within the serpentinized matrix and is sometimes Fe-rich with up to 27.34 wt% FeO.

At the bottom of Hole 1496A (core 3), some clasts were recovered that represent aspects of rodingitization. The ultramafic rock is highly serpentinized dunite and the preserved primary assemblage consists of mainly olivine and minor clinopyroxene as well as Cr-spinel (Figure 2f), whereas orthopyroxene is completely serpentinized. Olivine shows variable Mg# ranging from 83 to 92 (Table 3). Clinopyroxene has diopside composition with CaO of 22.15–24.03 wt% and MgO of 17.85–19.85 wt%. Spinel has high Cr# of 90 and rather low Mg# of 22–26 and the larger spinel grains display rather wide, up to 50 μm, coronas of magnetite (Figure 6a). Na-rich amphibole (richterite) was also detected in association with diopside (Figure 7b, Table 3). It contains up to 7.42 wt% Na_2O and its Al_2O_3 content ranges between 0.01 and 0.19 wt%. The chemical composition of serpentine minerals is homogenous throughout the matrix and veins (Figure 2b), with SiO_2 varying between 34.97 and 44.10 wt%

10.1029/2023GC010968

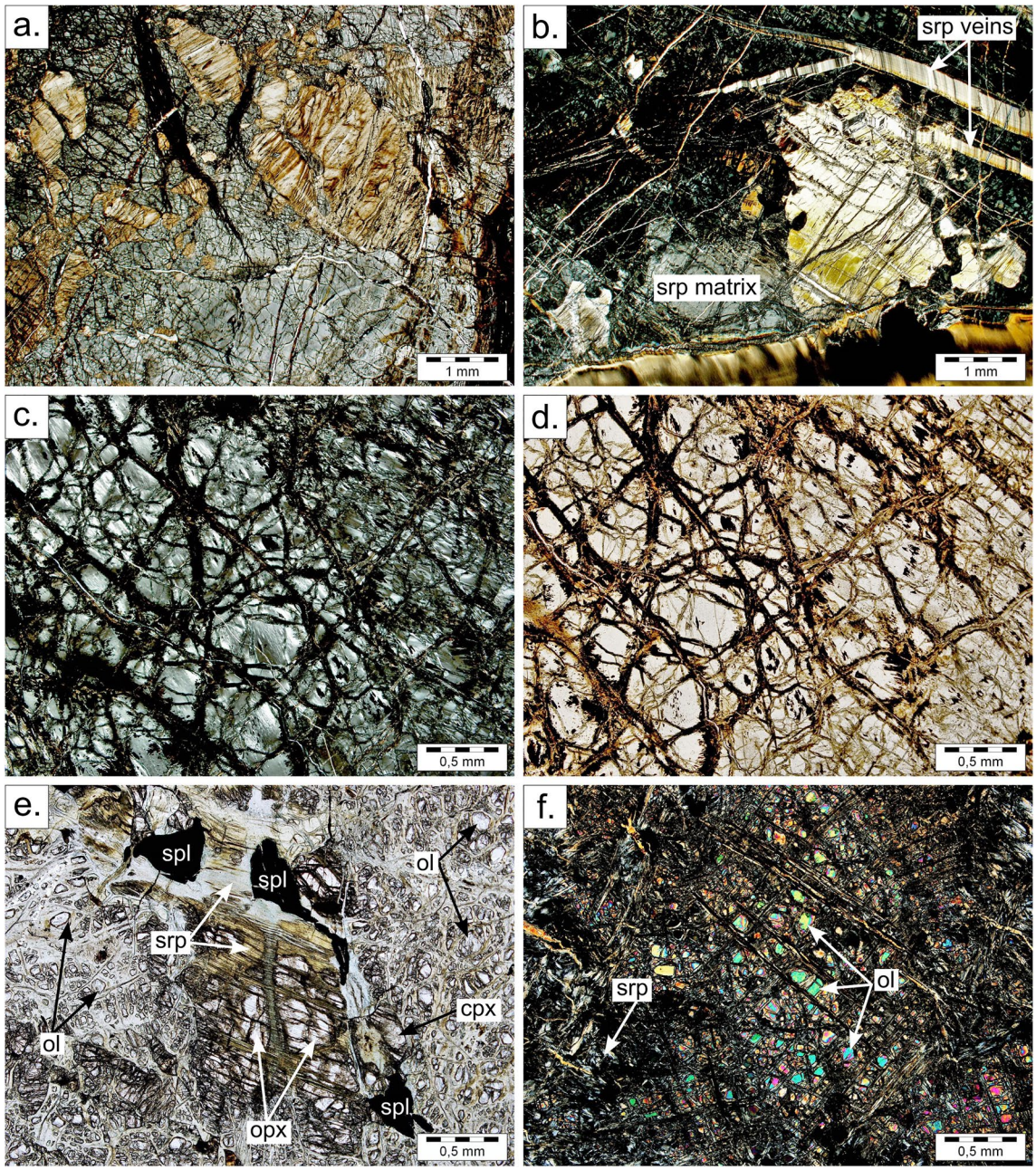

Figure 2. Thin section photographs of completely and partly serpentinized ultramafic rocks from Fantangisña and Asùt Tesoru Seamounts, respectively: (a) bastite texture (sample 1-1498B-210); (b) bastite texture with secondary veins (sample 1-1498B-224); (c) mesh and hourglass textures (sample 1-1498B-249); (d) mesh texture in reflected light (sample 1-1498B-249); (e) partly serpentinized harzburgite from the summit of Asùt Tesoru (sample 1-1496C-136); (f) partly serpentinized dunite from Asùt Tesoru (sample 1-1496A-100). Abbreviations: *cpx* clinopyroxene, *ol* olivine, *opx* orthopyroxene, *spl* spinel, *srp* serpentine.

and MgO of 37.80–40.79 wt%. FeO in serpentine is rather low and reaches up to 5.34 wt%. Brucite crystallizes mainly in veins but is also detected throughout the matrix. It has highly variable composition with MgO and FeO ranging from 35.98 to 55.26 wt% and 11.51 to 28.39 wt%, respectively.

In the same core, a clast was recovered consisting of up to c. 95% of garnet and c. 5% of chlorite (Figures 3b and 6b) and represents the reaction zone between rodingite and serpentinite. The garnet has variable andraditic composition with Al_2O_3 ranging from 0.51 to 13.65 wt% (Table 3). It is sometimes Ti-rich with TiO_2 reaching up to 13.40 wt%. The composition of chlorite is non-homogenous with MgO content ranging from 14.72 to 27.91 wt% and FeO of 9.36–29.11 wt% (Table 3). A brecciated rodingite clast was investigated and consists mainly

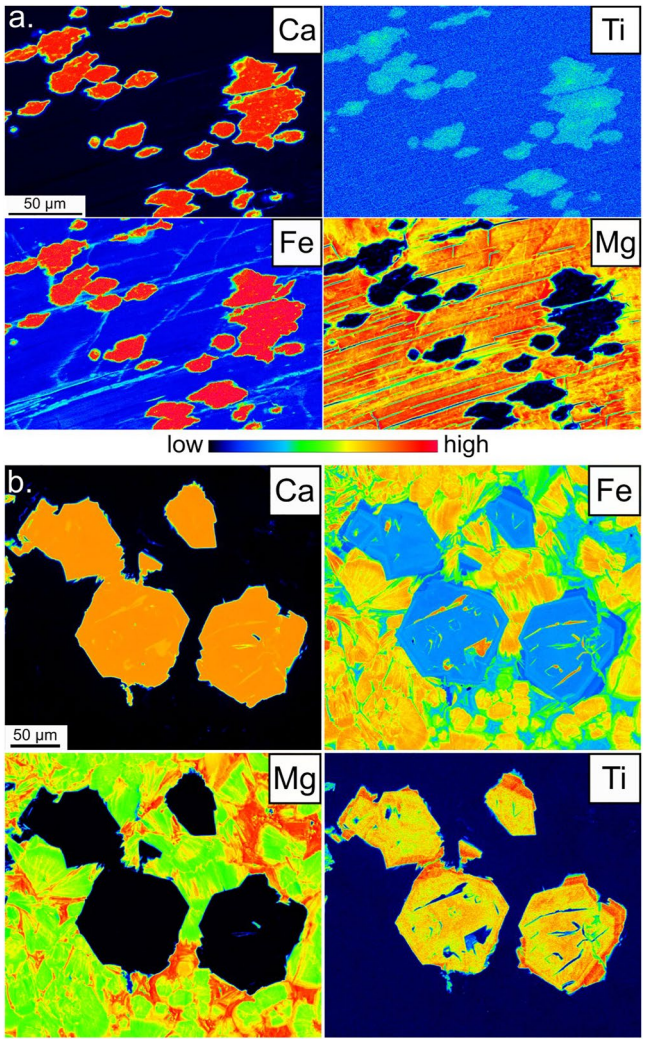

Figure 3. Major element distribution maps of representative garnet crystals from the investigated samples: (a) hydrogarnet with andradite composition in completely serpentinized ultramafic clast from Fantangisña Seamount (sample 1-1498B-249); (b) hydrogarnet with andradite composition and variable TiO_2 content in a sample representing the reaction zone between serpentinite and rodingite (sample TSB-73).

of clinopyroxene and titanite in a fine-grained matrix of chlorite and clay minerals. Large clinopyroxene clasts are diopside rich and show beginning stages of replacement by garnet along the cleavage (Figure 6c). Throughout the matrix, smaller prismatic clinopyroxene crystals have variable CaO content and, thus, are classified as either augite or diopside or wollastonite (Figure 7a, Table 3). Microscopic analysis of the veins revealed that they are also made up by clinopyroxene with the same chemical composition as in the matrix; however, they also contain large, up to 500 µm, crystals of titanite and apatite (Figure 6d). Compared to the reaction zone, chlorite composition in rodingite shows more variable SiO_2 content between 28.78 wt% and 35.45 wt% (Table 3). In contrast, in the chlorite from the reaction zone, FeO and MgO reach higher values of up to 29.11 wt% and 27.34 wt%, respectively. Additionally, the garnet in the rodingite shows a narrower compositional range than that in the reaction zone with TiO_2 ranging from 6.29 to 9.32 wt% (Table 3).

The investigated serpentine muds from Holes 1493B, 1494A and 1495B at the flank of Asút Tesoru Seamount show an overall continuous transition with sampling depth: (a) from dark blue towards bluish-green color, (b) from dominating clayey to sandy particle size, and (c) an increase in rock clast size. In general, the grain size of the serpentine mud is sandy to clayey with slightly varying proportions. The serpentine minerals form elongated and fibrous assemblages within the matrix with bastite and mesh textures. Also present in the samples are chlorite, magnetite, spinel, brucite, carbonates and hydrogarnet. Rare fragments of microfossils are most likely foraminifera filled with opaque pyrite. Interestingly, microcrystalline iowaite is only present in the samples from the flank sites (U1493, U1494, U1495) whereas it is completely absent at the summit. XRD analysis clearly identified its abundance at the upper parts of the drill cores, but its occurrence decreases with sampling depth (Figure 4b).

Recovered ultramafic clasts from the flank of Asút Tesoru Seamount show similar composition to the harzburgite from the summit. The degree of serpentinization is high, but the primary mineral composition is still preserved (Figure 6e, Table 3). Olivine has a high forsterite component (90.86–92.43) and is unzoned. The enstatite component in orthopyroxene ranges between 90.17% and 91.56%. Clinopyroxene is either augite or diopside ($En_{41.13\text{-}55.99}Wo_{32.99\text{-}47.58}$). Unzoned calcic amphibole (tremolite) with Al_2O_3 content ranging between 0.37 and 2.18 wt% and CaO varying from 12.35 to 12.99 wt% occurs together with the pyroxene (Figure 7b). Andraditic garnet occurs either in association with pyroxene or with amphibole. Two types of spinels occur: (a) Cr- and Fe-rich spinel with elevated Cr# of 67–77 but very low Mg# ranging from 13 to 16, and (b) Cr-rich spinel with Cr# varying between 42 and 49 and Mg# of 34–56. Both spinels display sometimes thin but well-developed magnetite corona textures. Serpentine composition is characterized by rather low SiO_2 (30.98–44.14 wt%) and MgO (33.95–41.43 wt%) but high FeO (up to 18.93 wt%, Table 3), which suggests the presence of brucite at microscale. Single-grained brucite is rare and Fe-rich (FeO <33.29).

A rare rock clast of ophicarbonate was recovered in hole U1493B (core 2; Figure 6f). The single aragonite crystals are rather large and commonly display a prismatic habit. Uncommonly, the crystals include hydrogarnet with almost pure andraditic composition (Table 3). Serpentine is less present in this sample and contains Cr-spinel relics as well as magnetite/hematite and Cr-rich garnet (Figure 6f, Table 3). The latter contains up to 23 mol% uvarovite component and at least 76.5 mol% andradite. It occurs in aggregates together with rare Fe-Cr oxides, which suggests that the garnets replace a former Fe–Cr–Al spinel. Cr-rich garnets with similar composition were observed also within the unlithified serpentine muds.

In general, all ultramafic clasts from Asùt Tesoru Seamount show a forearc peridotite signature (Figure 8). Specifically, chromite is able to maintain original magmatic characteristics due to its high resistance to fluid-driven

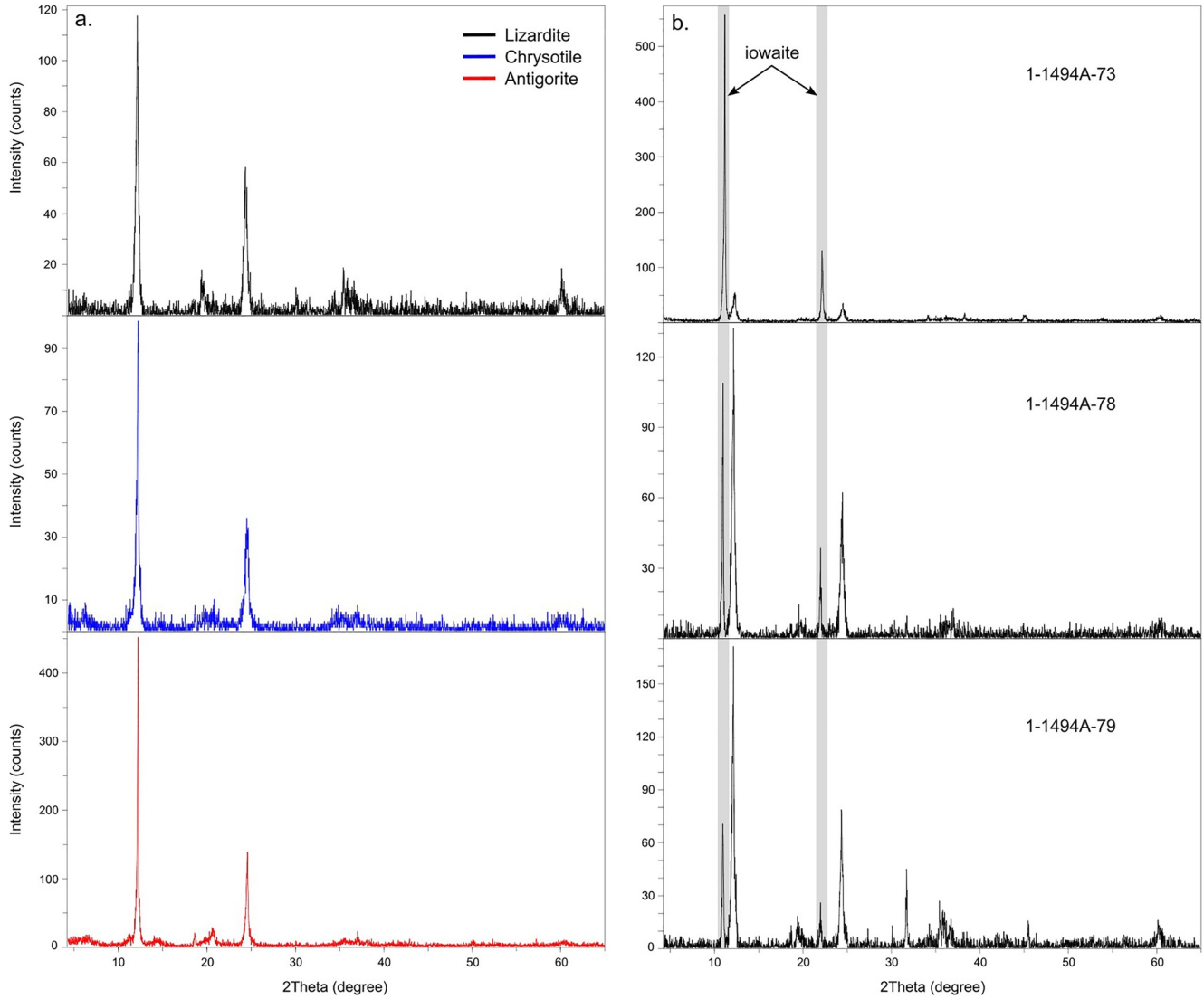

Figure 4. XRD patterns of (a) serpentine minerals in the investigated mud samples reveal the presence of the three serpentine modifications (lizardite, chrysotile and antigorite in samples 1-1494A-84, 1-1496B-125 and 1-1495B-95, respectively); (b) iowaite in the mud samples from the flank of Asút Tesoru Seamount shows a decrease in its occurrence with sampling depth (samples 1-1494A-73, 1-1494A-78 and 1-1494A-79).

alteration (e.g., Baumgartner et al., 2013). In the Mg versus Cr diagram, it was observed that the investigated samples fall into the forearc peridotites composition area (Figure 8a; Dick & Bullen, 1984; Ishii et al., 1992; Parkinson & Pearce, 1998; Sobolev & Danyushevsky, 1994). When the chromite mineral data are plotted in a Cr# versus TiO_2 diagram, it represents the forearc peridotite (Figure 8b; Bonatti & Michael, 1989; Dick & Bullen, 1984). The olivine mineral data also plot within the forearc peridotite zone on the Fo versus NiO wt% diagram (Figure 8d; Choi et al., 2008; Ishii et al., 1992; Johnson et al., 1990). According to the Al_2O_3 versus Cr_2O_3 diagram, orthopyroxene minerals are primary and once again plot within the forearc peridotite field (Figure 8e; Laouar et al., 2017).

4.3. Whole Rock Geochemistry

The bulk chemistry of seven representative serpentine mud samples was analyzed using X-ray fluorescence analysis in order to determine progressive serpentinization with potential element loss. The obtained data were compared and showed good agreement with the shipboard data (Tables T3 and T4 in Fryer et al., 2017). Displayed measurements include major element concentrations (SiO_2, MgO, CaO, Al_2O_3, Fe_2O_3, Na_2O in wt%) as well as

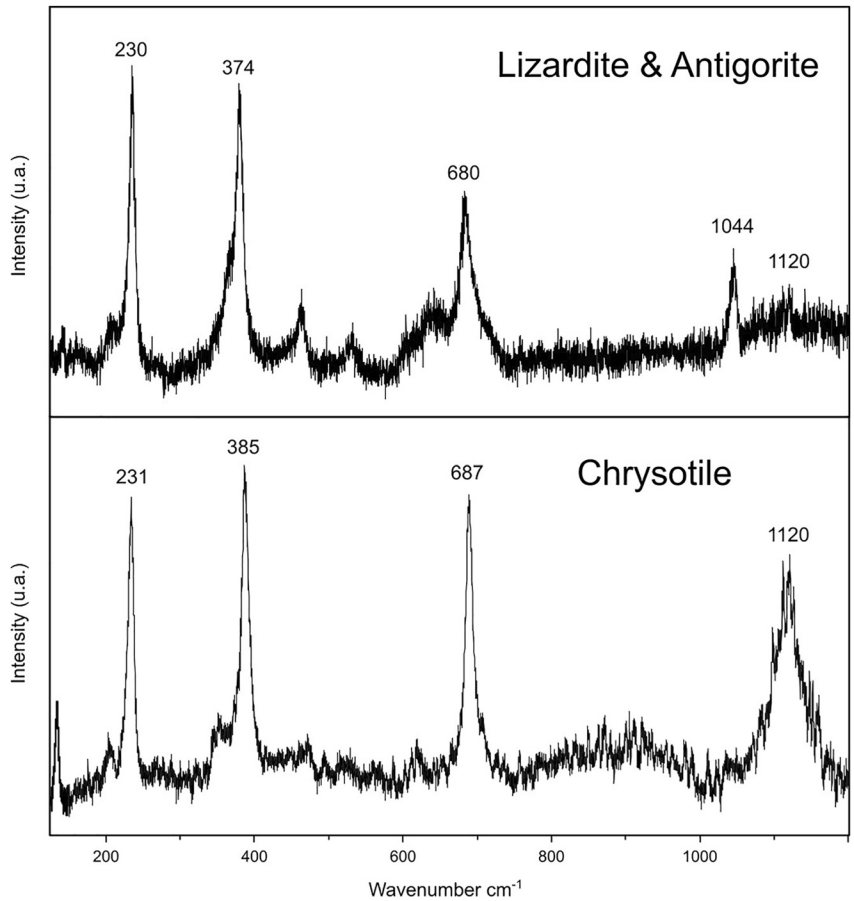

Figure 5. Raman spectra acquired from the different varieties of serpentine in the studied mud samples within the low frequency ranges (120–1,150 cm^{-1}). Mixed spectra show characteristic bands of lizardite and antigorite (230, 1,120 cm^{-1} and 374, 680, 1,044 cm^{-1}, respectively; sample 1-1496A-113). Raman spectrum of chrysotile includes a pronounced peak at 1,120 cm^{-1} (sample 1-1495B-89).

selected trace elements (Ni, Cr, V in ppm). Overall, the high LOI values (13.34–16.02 wt%; Table 2) indicate medium to high serpentinization degree of the mud samples. The contents of the most major oxides as well as Cr show minor variations, especially for SiO_2 (41.84–44.89 wt%), MgO (44.45–47.36 wt%) and Fe_2O_3 (7.79–8.39 wt%). Slight change can be observed in the CaO (0.00–0.87 wt%) and Ni (1791–2661 ppm) values, which may very well correlate to the presence/absence of clinopyroxene, since the samples with the lowest CaO (0.05 wt% in 1493B-61 and 0.00 wt% in 1494A-81) exhibit the highest Ni contents (2,492 ppm in 1493B-61 and 2,661 ppm in 1494A-81) and, thus, indicates dunitic nature for these samples.

The whole-rock composition of the investigated serpentine muds largely confirms the forearc peridotite signature of the protoliths as inferred by the mineral composition of the relatively well-preserved peridotites (Figures 8 and 9). Especially, their depleted composition in CaO and Al_2O_3 resembles that of forearc peridotites (Figure 9a). In a geotectonic sense, the investigated muds are comparable to typical SSZ-type peridotites (Figure 9b).

On variation diagrams, the strongest correlations are observed when major oxides as well as Ni and Cr are plotted against MgO (Figure 10). CaO, FeOt and MnO show a distinct negative covariance with MgO, whereas SiO_2 as well as Cr and Ni are positively correlated with the MgO contents of the muds (Figure 10). On the MgO/SiO_2 versus Al_2O_3/SiO_2 diagram, the investigated mud samples plot, similarly to previous studies of the nearby seamounts, at the depleted end of the mantle fractionation array (Figure 11; Hart & Zindler, 1986; Jagoutz et al., 1979), with relatively low Al_2O_3/SiO_2 (<0.02) and high MgO/SiO_2 (>0.99) ratios. This suggests that they

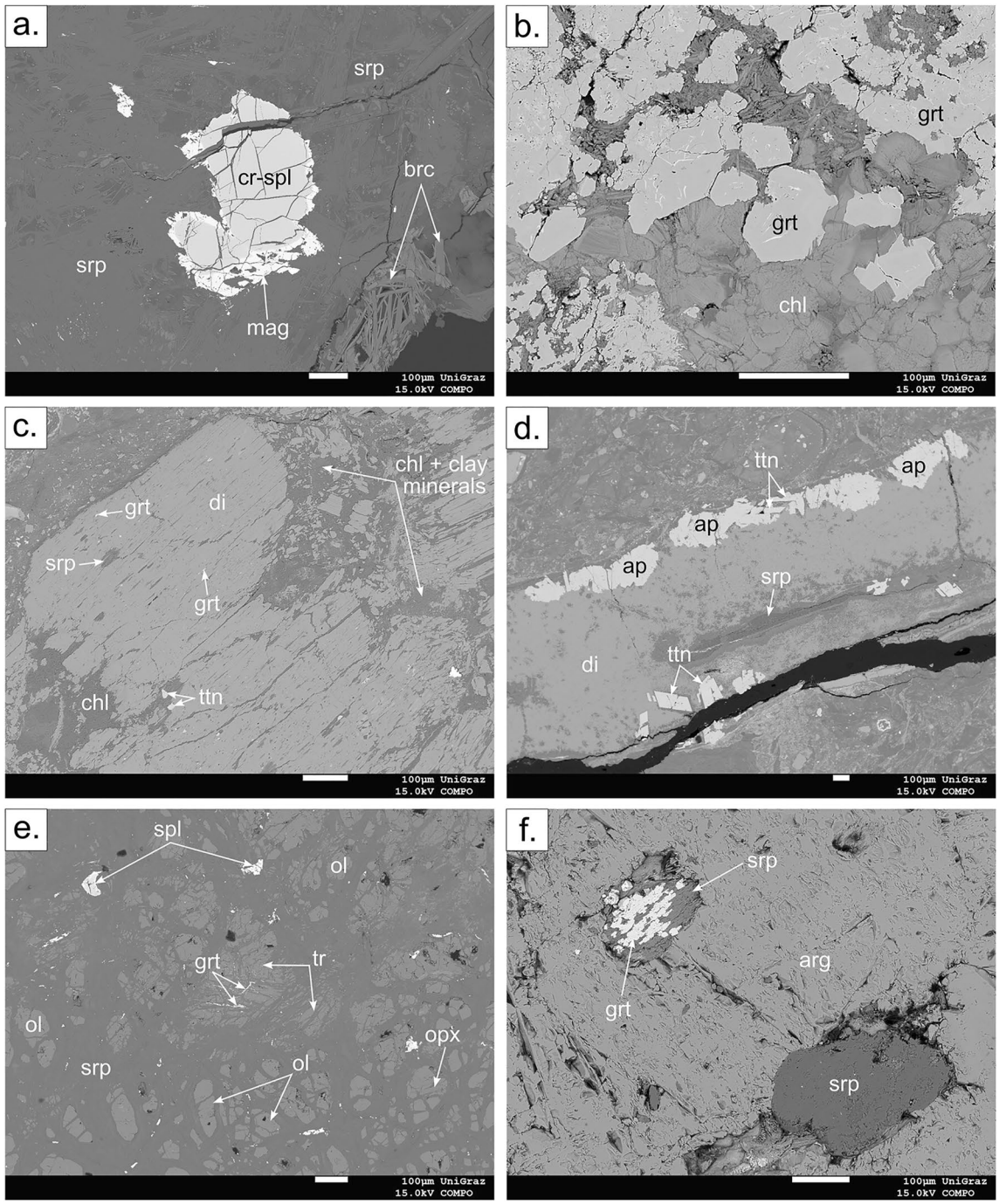

Figure 6. Back Scattered Electrons (BSE) images of representative samples: (a) Cr-spinel with magnetite corona in a serpentinized matrix (sample 1-1496A-100; (b) sample from the reaction zone between serpentinite and rodingite, containing mainly hydrogarnet with variable composition and chlorite (sample TSB-73); (c) rodingite (sample 1-1496A-102); (d) diopside-rich vein with idiomorphic titanite and apatite within rodingite (sample 1-1496A-102); (e) serpentinized peridotite from the flank of Asút Tesoru Seamount (sample 1-1493B-68); (f) recovered ophicarbonate clast from the flank of Asút Tesoru Seamount (sample 1-1493B-57). Abbreviations: *ap* apatite, *arg* aragonite, *brc* brucite, *chl* chlorite, *cr-spl* Cr-spinel, *di* diopside, *grt* garnet, *mag* magnetite, *ttn* titanite, *tr* tremolite.

have not lost any original Mg content due to secondary events, for example, MgO loss due to seafloor alteration and/or SiO_2 enrichment related to talc crystallization (Bach et al., 2004; Godard et al., 2008; Paulick et al., 2006; Snow & Dick, 1995). Samples that plot above the mantle array are typically dunites and olivine-rich harzburgites as reflected by high MgO/SiO_2 as well as increasing olivine/orthopyroxene ratios in the rocks.

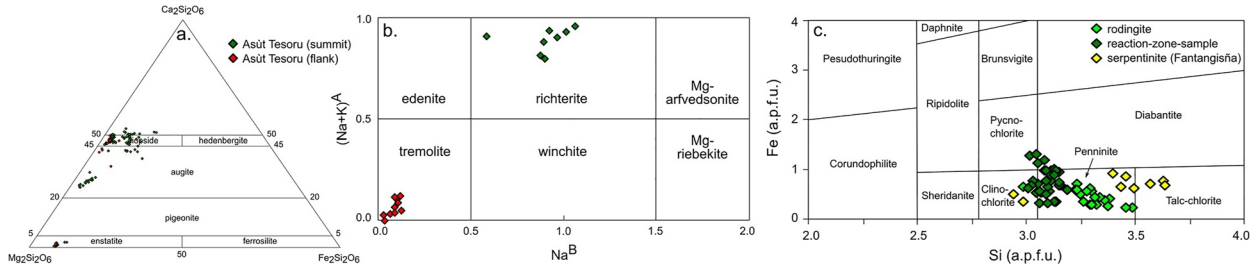

Figure 7. Mineral composition plots for the classification of (a) pyroxene, after Morimoto et al. (1988); (b) amphibole, after Meeker et al. (2003); and (c) chlorite, after Hey (1954).

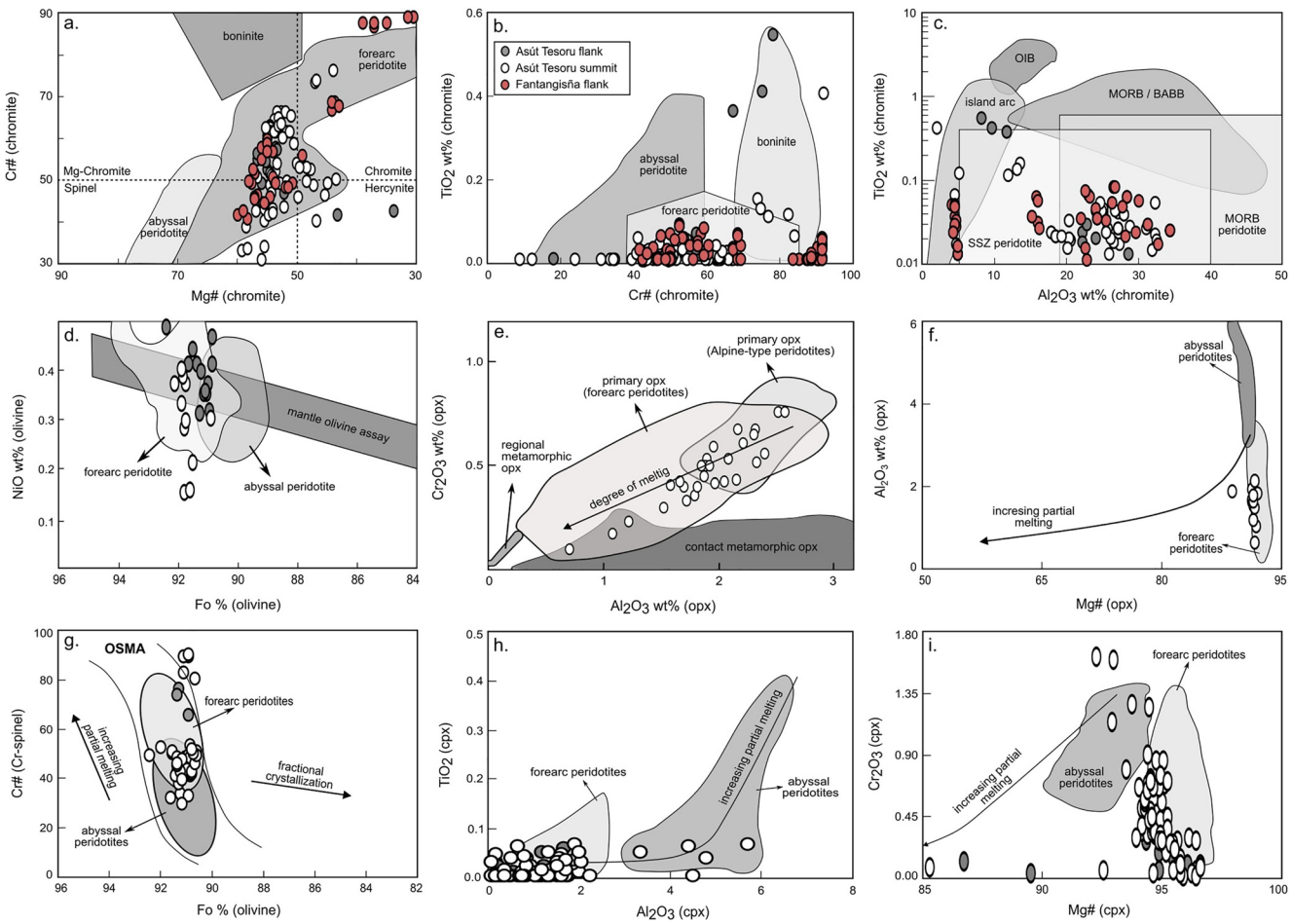

Figure 8. Diagram of (a) Mg# versus Cr# in Cr-spinels. Abyssal peridotite field is from Dick and Bullen (1984), forearc peridotite field is from Ishii et al. (1992) and Parkinson and Pearce (1998), boninite area is from Sobolev and Danyushevsky (1994); (b) Cr# versus TiO_2 (wt%) of Cr-spinels, to discriminate between various types of peridotites and boninite (Tamura & Arai, 2006); (c) tectonic discriminant diagram of TiO_2 (wt%) versus Al_2O_3 (wt%) in Cr-spinels (Kamenetsky et al., 2001); (d) Fo % versus NiO (wt%) in olivine. Fields are from Choi et al. (2008), Ishii et al. (1992) and Johnson et al. (1990); (e) Al_2O_3 (wt%) versus Cr_2O_3 (wt%) in orthopyroxenes. Fields are from Laouar et al. (2017); (f) Al_2O_3 (wt.%) versus Mg# in orthopyroxenes; (g) Cr# of Cr-spinel versus Fo % in coexisting olivine. Olivine-spinel mantle array and melting trend are from Arai (1994), abyssal peridotite field from Dick and Bullen (1984), forearc peridotite field from Ishii et al. (1992), Parkinson and Pearce (1998) and Pearce et al. (2000); (h) TiO_2 (wt%) versus Al_2O_3 (wt%) in clinopyroxene of the studied rocks. Fields for abyssal and forearc peridotites are from Hébert et al. (1990) and Johnson et al. (1990), and Ishii et al. (1992), respectively; (i) Cr_2O_3 (wt%) versus Mg# in clinopyroxene. Abyssal peridotite field is from Johnson et al. (1990), forearc peridotite field is from Ishii et al. (1992).

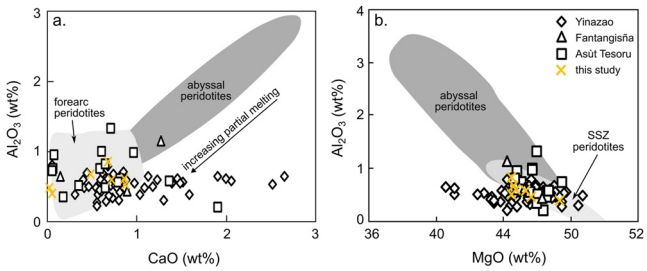

Figure 9. Whole-rock plots of the examined serpentinite muds: (a) Al_2O_3 (wt%) versus CaO (wt%). Abyssal and forearc peridotite fields are taken from Pearce et al. (1992); (b) Al_2O_3 (wt%) versus MgO (wt%). Abyssal and SSZ peridotite fields are from Niu et al. (1997) and Parkinson and Pearce (1998), respectively.

4.4. Chlorite Thermometry

Chlorite grains in two samples from Asùt Tesoru, a rodingite and a reaction-zone-sample, and one serpentinite sample from Fantangisña were analyzed using an electron microprobe. The mineral formula was recalculated based on 14 oxygen atoms per formula unit (a.p.f.u.). The results are plotted on the chlorite classification diagram after Hey (1954; Figure 6c).

Overall, the applied geothermometers estimated similar formation temperatures for the chlorites in each sample (Figure 12). Temperatures calculated by the thermometers of Cathelineau (1988) and Jowett (1991) show a difference of only ±7°C, whereas the thermometer of Cathelineau and Nieva (1985) shows slightly lower temperatures for the sample from the reaction zone and slightly higher in the chlorites from the serpentinite (Figure 12). The composition of the chlorite in rodingite indicates formation temperatures between 96° and 204°C (mean = 162°C). The temperature estimates from the sample from the reaction zone are clearly higher with variation between 193 and 270°C (mean = 228°C). The chlorite geothermometry yields the lowest formation temperatures of 51°–145°C (mean = 102°C) in the serpentinized ultramafic rock from Fantangisña, which correlates rather well with the overall low-grade serpentinization conditions at this seamount.

5. Discussion

Oceanic serpentinites usually consist solely of serpentine minerals and magnetite, which often makes unraveling of their magmatic and metamorphic history via fluid-mineral phase relationships difficult. In this regard, the serpentinites recovered during IODP Expedition 366 are quite remarkable, as they exhibit highly variable mineral composition. The clasts document progressive changes of metamorphic grade and degree of serpentinization with increasing distance from the trench, including several stages of serpentinization, the transition of lizardite to antigorite as well as the presence of blueschist-facies mineral assemblages only in the mafic clasts from the furthest Asùt Tesoru Seamount (e.g., Debret et al., 2019; Ichiyama et al., 2021), and reveal processes of fluid-rock interaction both within the subduction channel and along the exhumation pathways underneath the serpentinite seamounts (Figure 13).

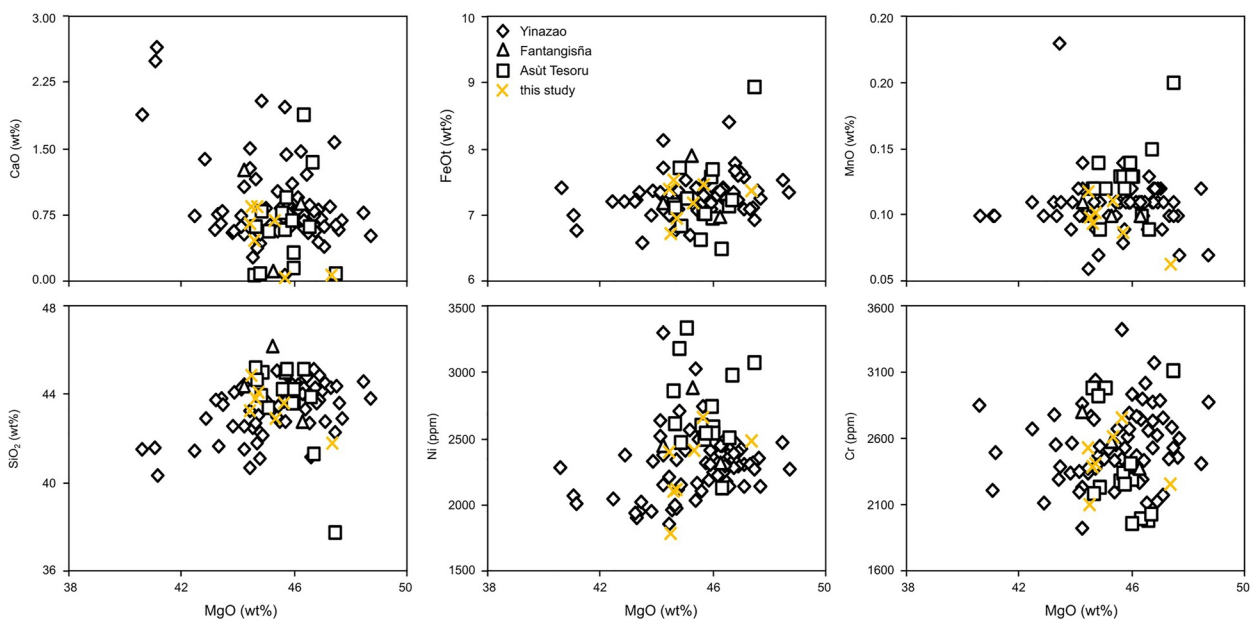

Figure 10. Variation diagrams of MgO (wt%) versus selected major oxide (wt%) and trace element (ppm) whole-rock abundances in the investigated serpentine muds.

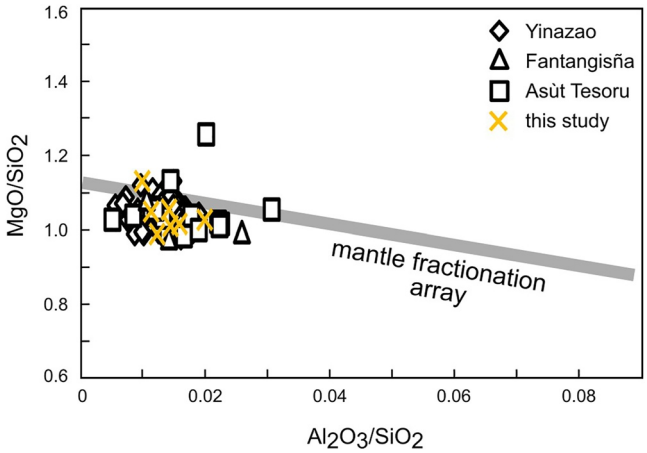

Figure 11. Whole rock major element ratios of MgO/SiO_2 versus Al_2O_3/SiO_2 for serpentinite mud samples from the Asùt Tesoru seamount. Samples are plotted with compiled shipboard data for serpentine muds from Yinazao, Asùt Tesoru and Fantangisña (Tables T3 and T4 in Fryer et al., 2017). "Mantle fractionation array" line after Hart and Zindler (1986) and Jagoutz et al. (1979).

5.1. Whole-Rock and Mineral Composition of Ultramafic Clasts

Due to the highly serpentinized nature of the investigated ultramafic clasts from Fantangisña Seamount it is difficult to infer their protolith based on the proportions and/or composition of olivine and pyroxene. However, Ichiyama et al. (2021) described serpentinized harzburgite and dunite, with minor relicts of olivine, Cr-spinel, orthopyroxene and clinopyroxene from the drill cores. The investigated ultramafic clasts from Asùt Tesoru Seamount exhibit lower degrees of serpentinization and are interpreted to be harzburgites, although rare dunites are also present. The generally low clinopyroxene abundances within the investigated peridotites provide direct evidence of the extent of depletion they have undergone, that is, they more resemble mantle peridotites which are formed by higher degrees of melting (e.g., Ahmed, 2013; Ishii et al., 1992; Parkinson & Pearce, 1998; Pearce et al., 2000; Uysal et al., 2012). The Al content in clinopyroxene is a sensitive indicator of the degree of mantle melting because it systematically decreases as peridotites grade of depletion increases (e.g., Uysal et al., 2012; Zhou et al., 2005). On the Al_2O_3 versus TiO_2 in clinopyroxene plot (Figure 8h), the studied mineral compositions fall in the field of clinopyroxenes from forearc peridotites, indicating that these rocks represent mantle residues after high degrees of partial melting under hydrous conditions (e.g., Kapsiotis, 2014).

Chromite minerals from mantle peridotites are another important indicator for characterizing the partial melting processes in the upper mantle (Parkinson & Pearce, 1998; Uysal et al., 2013). Because of differences in the crystallographic behavior, Ti fractionates out of chromite during partial melting. As a result, high Cr# values of chromite correlate positively with the degree of partial melting because they become richer in Cr with increasing degrees of depletion (Dick & Bullen, 1984; Irvine, 1965). Furthermore, together with the high Mg-nature of olivine, the data illustrate that the investigated peridotites fall in the forearc area on the olivine-spinel mantle array (OSMA) diagram with moderate to high degree of melt (Figure 8g; e.g., Khalil & Azer, 2008; Üner, 2021).

Taking into account that the investigated serpentine mud samples have retained their high MgO contents and, thus, have not been largely affected by seafloor weathering, the obtained whole-rock data indicate no significant changes in the original bulk chemistry. Moreover, it is in very good agreement with the mineral composition data from the lithic serpentinite clasts. In particular, Al_2O_3, CaO and MnO show a negative correlation with MgO (Figures 9b and 10), which suggests that they are preferentially enriched in a melt generated after partial melting of the mantle. On the other hand, Ni concentrations are positively correlated with MgO (Figure 10), which is related to its compatible behavior in olivine during mantle melting (e.g., De Hoog et al., 2010; Sato, 1977).

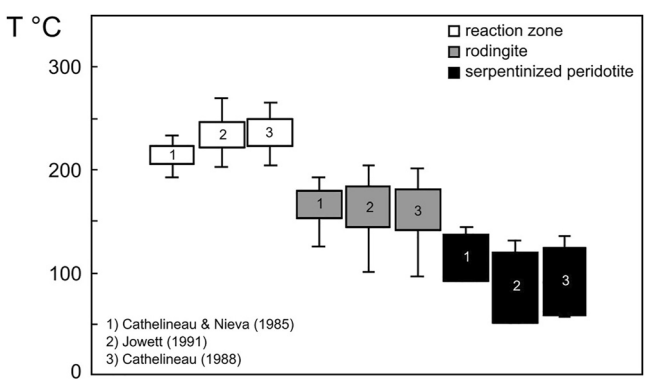

Figure 12. Box plot of the calculated temperatures of chlorites from the reaction zone (white boxes), rodingite (gray boxes) and serpentinized ultramafic rock from Fantangisña (black boxes), based on the geothermometers of Cathelineau and Nieva (1985), Cathelineau (1988) and Jowett (1991).

Summarily, according to their petrography and mineral composition, the clinopyroxene-bearing ultramafics show depleted signatures, indicating that they are residues after moderate to high degrees of partial melting. Their degree of depletion is particularly attested by (a) the generally low modal amount of clinopyroxene, (b) the low Al_2O_3 and Cr_2O_3 contents in pyroxenes, (c) the high Fo values in olivine, and (d) the relatively high Cr# in Cr-spinels.

5.2. Serpentinization

The complex metamorphic evolution of oceanic serpentinites and associated gabbros from various settings has been investigated by numerous studies (e.g., Agrinier & Cannat, 1997; Agrinier et al., 1995; Bideau et al., 1991; Dilek et al., 1997; Hébert et al., 1990; Mével et al., 1991; Prichard, 1979; Schroeder et al., 2002). It includes high-temperature (>300°–400°C) serpentinization and rodingitization (Figure 13a) as well as multiple lower-temperature overprints related to exhumation and exposure of the mantle at the seafloor. Generally, serpentinites have remarkably uniform composition, consisting of

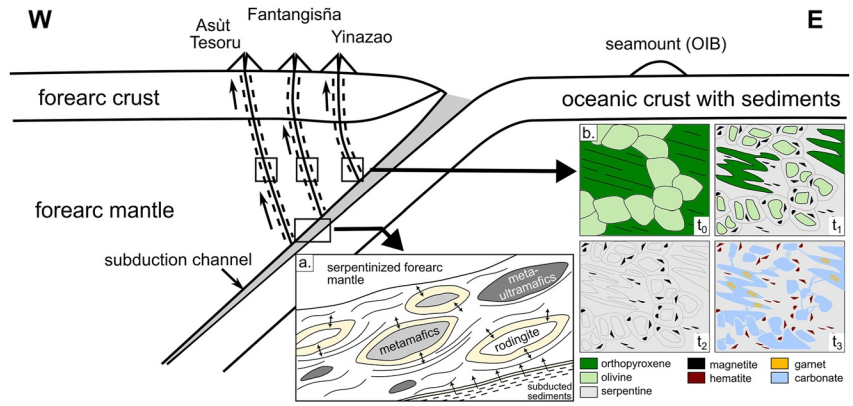

Figure 13. Tectonic sketch illustrating the Mariana subduction zone. Not to scale: (a) cartoon showing the subduction channel below the Mariana forearc, where metasomatic reactions (yellow areas) between serpentinite and lithologies derived from the subducting slab as well as from the forearc mantle are taking place. These are associated with aqueous fluids from different sources (black arrows), including fluids released by dehydrating of the subducted slab or during metamorphic reactions; (b) cartoon illustrating the sequence of hydration and carbonation processes leading to the formation of ophicarbonate (modified after Cannaò et al., 2020). A fresh mantle peridotite is sketched at t_0. Hydration and alteration of pyroxene and olivine (t_1) takes place after interaction with aqueous fluid, leading to their complete hydration (t_2). Carbonation of the hydrated mantle minerals (t_3) may occur after change of the redox conditions and interaction with CO_2-enriched fluids. The three boxes in the mud volcano conduits indicate that these processes may take place in any of them.

serpentinite polytypes and magnetite, and eventually brucite, talc and/or tremolite (e.g., Mével, 2003). Additionally, their metamorphic stability field is large (e.g., Evans, 2004). Thus, the temperature-pressure stabilities of serpentine phases are not well constrained. According to thermodynamic calculations antigorite is the stable serpentine phase above 200–300°C and pressures below 2 kbar and chrysotile and lizardite form from antigorite during low-temperature recrystallization (e.g., Evans, 1977). However, more recent field studies (e.g., O'Hanley & Wicks, 1995), hydrothermal experiments (e.g., Allen & Seyfried, 2003; Janecky & Seyfried, 1986; Normand et al., 2002) as well as stable isotope studies (e.g., Agrinier & Cannat, 1997; Agrinier et al., 1995; Früh-Green et al., 1996) revealed that lizardite and chrysotile may form directly from olivine at temperatures above 300°C.

In the greenschist and low-temperature blueschist facies (from <300° to 360°C), lizardite and locally chrysotile are the dominant types in the mesh texture (Andreani et al., 2007; Evans, 2004; Schwartz et al., 2013). In the middle-temperature blueschist facies, between 320° and 390°C, lizardite is progressively replaced by antigorite in the cores of the lizardite mesh, but also at the grain boundaries via dissolution–precipitation processes in the presence of free, SiO_2 enriched fluids (Lafay et al., 2012; Putnis, 2009). In the high-temperature blueschist and eclogite facies (T > 380°C), antigorite ultimately becomes the sole serpentine type. Chrysotile is usually observed in high-pressure serpentinite samples, filling in the late cracks or micro-fractures related to final exhumation at the ductile/brittle transition (Schwartz et al., 2013).

Within the investigated serpentinites, lizardite is the dominant phase and antigorite is virtually absent, which suggests sub-greenschist facies metamorphic conditions at P < 4 kbar and T ~200°–300°C. However, Raman spectroscopy reveals mixed lizardite/antigorite spectra (Figure 5), suggesting the association of lizardite and antigorite at the micron-scale. According to Putnis (2009), a mixed spectrum of these two phases occurs during the partial replacement of one phase by another during dissolution—re-precipitation processes. The crystallization of antigorite at the expense of lizardite takes place between 340° and 380°C at 4 kbar (Schwartz et al., 2013) following the H_2O-conserved reaction of Evans (2004):

$$17\,Mg_3Si_2O_5(OH)_4\,(lz/ctl) = Mg_3Si_2O_5(OH)_4\,(atg) + 3\,Mg(OH)_2\,(brc) \quad (1)$$

The presence of incompletely serpentinized ultramafic rocks (i.e., meta-ultramafics; Figure 13a) provides additional insight into the reaction pathways during serpentinization processes. According to previous studies, serpentinization at low to moderate temperature (<250°C) is a nonequilibrium process, during which olivine reacts faster than pyroxene and the precipitation rates of talc are very low (e.g., Bach et al., 2004; Martin & Fyfe, 1970; Nesbitt & Brickner, 1978). Under these conditions, olivine would break down to form serpentine, magnetite and brucite. This reaction, which is widely observed in the investigated samples from Fantangisña

Seamount, will be ongoing in the presence of moderate-temperature subduction-channel fluid. The effect of pyroxene on the solution chemistry, that is, its replacement by talc and tremolite and the formation of serpentine, takes place at temperatures above 350°C (e.g., Allen & Seyfried, 2003; Janecky & Seyfried, 1986; Martin & Fyfe, 1970). In this case the high-temperature slab-derived fluid that is required for these reactions needs to be pyroxene saturated, has low pH and the silica activity is high (e.g., Allen & Seyfried, 2003). Additionally, it is enriched in Ca, Si, H_2 and acidity so it may cause rodingitization in adjacent basic magmatic bodies (Bach et al., 2004). Furthermore, the presence of relatively fresh to slightly altered orthopyroxenes in the harzburgites and dunites from Asùt Tesoru Seamount suggests that these rocks reacted with a rather high-temperature slab-derived fluid (>300°C), since orthopyroxene would react faster than olivine under these conditions (e.g., Bach et al., 2004).

However, many completely serpentinized peridotites lack talc and/or brucite because after pyroxenes are exhausted, the system moves toward lower silica activities so that talc reacts to form serpentine. This is supported by the occurrence of hydrogarnet (andradite) in the investigated samples together with serpentine + magnetite ± brucite ± Fe-Ni alloys. Andradite is highly sensitive to the silica activity and may form from diopside by the following reactions:

$$3\,Fe_3O_4\,(mag) + 12\,CaMgSi_2O_6\,(di) + 12\,H_2O\,(fluid) = 4\,Ca_3Fe_2Si_3O_{12}\,(adr) + 12\,Mg(OH)_2\,(brc) + Fe\,(alloy) + 12\,SiO_2\,(fluid) \quad (2)$$

$$3\,Fe_3O_4\,(mag) + 12\,CaMgSi_2O_6\,(di) + 8\,H_2O\,(fluid) = 4\,Ca_3Fe_2Si_3O_{12}\,(adr) + 4\,Mg_3Si_2O_5(OH)_4\,(srp) + Fe\,(alloy) + 4\,SiO_2\,(fluid) \quad (3)$$

$$3\,Fe_3O_4\,(mag) + 12\,CaMgSi_2O_6\,(di) + 6\,Mg(OH)_2\,(brc) + 6\,H_2O\,(fluid) = 4\,Ca_3Fe_2Si_3O_{12}\,(adr) + 6\,Mg_3Si_2O_5(OH)_4\,(srp) + Fe\,(alloy) \quad (4)$$

Reaction 4 marks the point where the system is buffered by the assemblage serpentine—brucite—diopside—magnetite, and andradite becomes the stable Ca phase in the serpentinite. The temperature of this intersection is dependent on the Ca content and pH of the ambient fluid, but for the most fluid compositions, it lies between 200 and 230°C (Frost & Beard, 2008). In the investigated samples, the assemblage serpentine—brucite—andradite—magnetite—alloy prevails, which suggests that Reaction 4 controls the occurrence of hydrogarnet in the rocks.

The occurrence of the brucite-serpentine assemblage in the investigated samples indicates low formation temperatures in the absence of pyroxene. It also suggests that the circulating fluids had relatively high pH and the silica activity was low. Hence, the formation of brucite may be expressed by the following reaction:

$$2\,Mg_2SiO_4\,(ol) + 3\,H_2O\,(fluid) = Mg_3Si_2O_5(OH)_4\,(srp) + Mg(OH)_2\,(brc) \quad (5)$$

Thus, the presence of both brucite and partially serpentinized pyroxene in some samples suggests local disequilibria during the main stage of serpentinization. Alternatively, the formation of the assemblage serpentine-brucite after olivine may have taken place at a later stage, when olivine is exhausted from the system and the hydration of serpentine to brucite drives the silica activity to higher values.

Formation of magnetite is suggested to represent the culmination of serpentinization and, thus, the assemblage serpentine-magnetite is common in rocks that lack or contain very little brucite, or rather rocks that have experienced a significant amount of hydration (Bach et al., 2006; Hostetler et al., 1966). Magnetite is abundant in the completely serpentinized peridotites from the Fantangisña Seamount, but it's rather rare in the incompletely serpentinized rocks from Asùt Tesoru Seamount, suggesting that its formation does not begin until very high levels of alteration of the primary rock are reached. Additionally, the amount of magnetite formed is controlled by the degree of Fe-incorporation to secondary phases (Bach et al., 2004; Frost & Beard, 2008), which means that it may not form at all if Fe-rich brucite and serpentine are formed, as observed in the serpentinized ultramafics from Asùt Tesoru Seamount (Figure 13b). Furthermore, the presence of hematite and iowaite indicates that seawater-rock interaction continued under fairly oxidizing conditions after serpentinization was largely completed.

Iowaite has already been described in ODP drill cores of serpentinite mud volcanoes in the Izu-Bonin forearc (Heling & Schwarz, 1992). It is thought to have formed from Fe-bearing brucite, when Fe^{2+} is oxidized to Fe^{3+}

and the generated charge imbalance is compensated by Cl^- from the seawater. It has been proposed that this reaction takes place immediately below the seafloor due to infiltration of seawater, which might explain the decreasing presence of iowaite in the investigated mud samples from the flank of Asùt Tesoru Seamount with sampling depth.

In sum, incompletely serpentinized ultramafic rocks (Figure 13a) provide information on the metamorphic overprint at comparably higher grade, potentially within the subduction channel pathways during serpentinization processes. The secondary mineral paragenesis of the serpentinites, including mainly lizardite and chrysotile serpentine group minerals, along with brucite as well as andradite, and the apparent absence of high-temperature phases such as antigorite and anthophyllite, tentatively constrains an upper temperature limit of 200°–300°C (e.g., Evans, 2004; Frost & Beard, 2008). However, as a fine-grained matrix of antigorite associated with lizardite can still be observed, suggesting a metamorphic temperature of at least 340°C. Altogether, these secondary assemblages seem to reveal the reaction processes during the ascend to the seafloor, that is, from higher to lower grade conditions, along the fault-related fractures within the forearc lithosphere acting as feeders for several serpentinite mud volcanoes (Figure 13b).

5.3. Rodingitization

Rodingitization is a metasomatic process involving CaO-rich, but SiO_2^-, Na_2O^-, and K_2O-poor rocks and, thus, it is often regarded as Ca-metasomatism (Coleman, 1967). It is usually associated with mafic rocks, including gabbros (e.g., Honnorez & Kirst, 1975; Kobayashi & Kaneda, 2010; O'Brien & Rodgers, 1973), basalts (e.g., Coleman, 1967; Evans, 1977) and diorites (Hatzipanagiotou & Tsikouras, 2001). The process occurs when the mafic and ultramafic rocks undergo the same metamorphic history, in which the Ca-rich fluids generated during serpentinization metasomatize the gabbros or basalts replacing pyroxene and plagioclase by Ca-Al and Ca-Mg silicates, such as diopside, tremolite, zoisite, prehnite and grossular/hydrogrossular (e.g., Bach & Klein, 2009; O'Hanley, 1996; Schandl et al., 1989). Other phases are usually vesuvianite and chlorite. During rodingitization, the interacting fluids become alkaline, with high-Ca and low-Si compositions (Frost & Beard, 2008; Janecky & Seyfried, 1986; Seyfried & Dibble, 1980; Seyfried et al., 2007). Under these conditions diopside and garnet increase their stability and rodingites act as Ca traps (Bach & Klein, 2009). Hence, they occur in a range of tectonic settings, mostly from the seafloor (e.g., Austrheim & Prestvik, 2008; Frost et al., 2008; Honnorez & Kirst, 1975; Li et al., 2007; Schandl et al., 1989).

In many cases, rodingites undergo several stages of metamorphism and metasomatism as well as secondary metamorphic overprint (e.g., Frost, 1975; Li et al., 2004; O'Hanley et al., 1992; Schandl et al., 1989). Additionally, during later stages they might actually lose Ca due to a reverse mass transfer, which makes it difficult to discern their pressure and temperature stabilities, especially in terms of specific mineral-fluid equilibria. Different studies suggest that this metasomatic event may occur at pressures between 0.25 and 3 kbar (Mittwede & Schandl, 1992; O'Hanley et al., 1992; Schandl et al., 1989). According to Bach and Klein (2009), the formation of the typical rodingite assemblage of grossular + diopside ± chlorite tales place at 200° and 300°C, but only in areas where the composition of the fluid is controlled by serpentinization reactions.

The synchronous rodingitization with serpentinization can be expressed by a hydrolysis reaction of diopside in serpentinite:

$$CaMgSi_2O_6\,(di) + 12\,H^+ = Ca^{2+} + Mg^{2+} + 2\,Si^{4+} + 6\,H_2O \quad (6)$$

This reaction will evolve the Ca^{2+} necessary for rodingitization of the mafic rocks, where the pyroxene and plagioclase are replaced by their hydrated chemical equivalents, that is, hydrogarnet, zoisite, wollastonite, chlorite, and amphibole. The presence of serpentine minerals in the fine-grained matrix suggests that the protolith may have contained olivine.

The common garnet phase in rodingites is hydrogarnet, in which $[(OH)_4]^{4-}$ substituted for $[SiO_4]^{4-}$. Typically, it contains up to 3 wt% of H2O (Honnorez & Kirst, 1975; O'Hanley et al., 1992; Schandl et al., 1989), which is also what we observed in the course of this study. However, the H_2O content can go up to c. 7 wt% in the investigated Ti-rich garnets from the reaction zone (Figures 3b and 7b; Table 3). Interestingly, some of these garnets exhibit a chemical zonation that resembles oscillatory zoning. This is commonly observed in metasomatic garnets where

the infiltrated fluid phase is in disequilibrium with the existing assemblage (e.g., Ortoleva et al., 1987; Yardley et al., 1991). According to Jamtveit et al. (1995) the differences in aqueous complexation behavior between Al and Fe in an aqueous solution increases the sensitivity of grandite (grossular + andradite) compositions to variations in temperature, pH, f_{O2} and to a lesser extent pressure. Assuming that the Fe haven't been substantially mobilized during rodingitization, most of the Fe^{2+} would have been rather oxidized to Fe^{3+}, which is compatible with the relatively high Fe^{3+} contents not only in garnets but in the bulk chemistry of the rodingite and reaction zone as well (Hatzipanagiotou & Tsikouras, 2001).

According to the thermodynamic reaction path models of Bach and Klein (2009) the mineral assemblage sequence at 200°C is clinopyroxene + garnet -> clinopyroxene + garnet + chlorite -> clinopyroxene + garnet + chlorite + prehnite -> clinopyroxene + prehnite + chlorite + tremolite. With increasing reaction progress, the initial Si concentrations as well as Ca in garnet increase, chlorite becomes more ferroan as visible in the chlorites from the reaction zone (Figure 6c), whereas clinopyroxene and tremolite retain their initial Mg content. At 300°C, the calculated mineralogical transitions proceed according to the following path: clinopyroxene (+garnet) -> garnet (+clinopyroxene, +chlorite) -> clinopyroxene + epidote/zoisite (+chlorite, +garnet). Garnet shows a large increase in X_{Al}, while clinopyroxene and tremolite are magnesian throughout. At ≥400°C, the assemblage is dominated by chlorite and garnet is not predicted to form at all. The applied chlorite geothermometry in our study on samples from the rodingite and reaction zone derived a chlorite formation temperature of max. 270°C in the presence of garnet and clinopyroxene, which confirms the results of Bach and Klein (2009).

Working on the assumption that rodingitization and serpentinization take place contemporaneously during progressive burial within the subduction channel (Figures 13a) and Frost and Beard (2008) highlighted the crucial role of silica activity in the process of rodingitization. According to their study, the silica activity of the brucite-serpentine equilibrium provides the drive for the reaction transforming anorthite and diopside to grossular and chlorite. At a pressure of 0.5 kbar, rodingitization takes place at temperatures around 200°–300°C in the presence of serpentinization fluids controlled by the brucite-serpentine-diopside equilibrium. At 400°C and above, brucite is absent, the fluids are buffered by serpentine-tremolite-talc and the silica activity is too high to allow rodingitization reactions to take place (Bach & Klein, 2009). In the study area, only the subduction channel environment can provide the described conditions since the pressures in the mud volcano conduits are not sufficient for the process to take place. Thus, we interpret the rodingitization to be related to progressive burial during subduction, as indicated in Figure 13a.

The mineral assemblages at the contact between mafic and ultramafic rock appear to have been largely affected by temperature. Monomineralic lithologies at the contact and within veins in rodingites are common (e.g., Honnorez & Kirst, 1975; Python et al., 2007; Schandl et al., 1989), where only the phase with the highest degree of supersaturation will precipitate (Korzhinskii, 1968). This is in line with the observations within the studied samples, which exhibit a garnet-rich reaction zone around a rodingite containing diopside-rich veins (Figures 7b and 7d). Furthermore, Schmitt et al. (2019) discussed the formation of titanian andradite in rodingite and recognized that it partly replaces perovskite and ilmenite under oxidizing conditions. The absence of any TiO_2-bearing minerals in association with garnet in our samples suggests a rather advanced stage of rodingitization, where the protolith has been completely overprinted by rodingite assemblages.

Finally, the textural and mineral observations in the investigated samples, including the progressive occurrence of antigorite, which is rare in oceanic serpentinites (Bach & Klein, 2009), as well as the transition of lizardite to antigorite, suggest that the main serpentinization event together with rodingitization took place during subduction, when fragments of the upper plate forearc mantle were incorporated within the subduction channel (Figure 13a). During their ascent within the mud volcanoes, some of the investigated samples were subjected to secondary alteration processes, leading to the formation of secondary serpentine veins in the serpentinites as well as clay minerals in the rodingites.

5.4. Ophicarbonates

Ophicarbonates, also referred to as carbonated ultramafic rocks, form when calcite recrystallization and carbonation of serpentinite clasts occur. Often the process takes place at the sea floor, causing low-to moderate temperature serpentinization of peridotites (e.g., Mével, 2003; O'Hanley, 1996) and the carbonation is powered by mixed seawater and alkaline hydrothermal fluids (e.g., Früh-Green et al., 2004; Ludwig et al., 2006).

However, ophicarbonates may also form within subduction channels, where (meta-)serpentinite is interacting with carbonic fluids. In this case, two processes are developing: (a) carbonation of the rock-forming silicates, and (b) C sequestration into the oceanic slab as well as the supra-subduction mantle (Piccoli et al., 2016; Scambelluri et al., 2016). According to experimental and thermodynamic modeling C in subducting oceanic crustal rocks remains relative immobile up to high pressure and temperature conditions, unless the rocks are infiltrated by externally derived hydrous fluids (e.g., Collins et al., 2015; Epstein et al., 2020; Molina & Poli, 2000; Poli et al., 2009). A convenient source is serpentinite, which supplies H_2O to adjacent carbonate rocks as a result of antigorite dehydration, and potentially leads to destabilization and dissolution of carbonates (e.g., Scambelluri et al., 2019). Furthermore, serpentinite is reactive to C-O-H fluids and is able to sequester CO_2 from the fluid via carbonation of its own silicate minerals (Scambelluri et al., 2016).

The ophicarbonate clast studied here displays a brecciated texture consisting of serpentinite clasts with different sizes in a coarse-grained aragonite matrix (Figure 7f). It is embedded within fine-grained serpentinite mud, which contains elongated and fibrous serpentine minerals, mesh and bastite as well as abundant magnetite, sometimes chromite and hydrogarnet. An ultramafic clast containing a well-preserved assemblage of olivine, ortho- and clinopyroxene, chromite and magnetite represents the ultramafic protolith of the investigated ophicarbonate (t_0 to t_2 in Figure 13b).

Whether or not the mantle protolith was serpentinized prior to carbonation is challenging to determine from a single clast. However, the presence of already serpentinized clasts within a carbonate matrix suggests that aragonite formation took place after the production of the mesh and bastite textures (t_3 in Figure 13b). In this case the input of Ca and CO_2 happens in an open system, where also Si, Mg and water (as hydroxyl molecules—OH^-) are released into the slab-derived fluid. According to thermodynamic modeling conducted by Klein and Garrido (2011), the serpentine replacement by carbonates occurs at 100°C and 0.5 kbar at a high CO_2 activity. This was confirmed by an experimental study by Grozeva et al. (2017), which showed that the formation of Ca- or Mg-rich carbonates after serpentinization of peridotite is related to the activity of Mg^{2+} in the fluid as well as to the presence of relict mantle minerals. In this case, the absence of Mg-rich carbonates such as magnesite and dolomite in the investigated ophicarbonate clast indicates that the slab-derived fluids reached Mg^{2+} saturation only after full consumption of the aqueous CO_2. These conditions indicate a different tectonic setting for the formation of the ophicarbonate compared to serpentinites that are associated with rodingite, that is, on the exhumation path within the serpentinite mud flow (Figure 13b).

As already established, hydrogarnet is a common secondary hydrothermal mineral phase in the studied samples and it defines a serpentinization temperature of c. 230°C (Frost & Beard, 2008). Garnet crystals with subhedral habit and almost pure andraditic composition are found within the carbonate matrix (Table 3). However, Cr-rich garnets are also common within the serpentinite clasts (Figures 7f and Table 3). They are subhedral to anhedral and contain chromite inclusions with similar composition to the unaltered chromites in the same sample. These textural observations suggest a secondary origin for the Cr-rich garnets as well, most probably related to subduction-channel fluids that infiltrated the ultramafic protolith. The formation of Cr-rich garnet after Cr-rich spinel is usually associated with hydrothermal or metasomatic reactions, although the precise mechanism of formation remains unclear (Arai et al., 1999; Ghosh & Morishita, 2011; Proenza et al., 1999). According to the studies of Ganguly (1976) and Melcher et al. (1997) Cr-rich hydrogarnets in serpentinites crystallize below 400°C, which is in line with the estimated metamorphic conditions and indicate an overall evolution of a subduction-channel fluid from c. 350°C (antigorite in serpentinites) to c. 100°C and below (chlorite in rodingite).

The identified trend of decreasing serpentinization temperature and increasing alteration degree with increasing proximity to the trench, that is, from Asùt Tesoru to Fantangisña, may be related to the enhanced fluid release during metamorphic reactions (e.g., the transition from lizardite to antigorite) as well as the long residence time of fluids within the shallower parts of the subduction zone. Additionally, the high degree of hydrothermal circulation in this zone contributes to the element cycling and, thus, the complete consumption of the primary mineral assemblages.

6. Summary and Conclusions

A variety of rock samples were recovered during IODP Expedition 366 along the Mariana Trench, where three serpentinite mud volcanoes at increasing distances from the trench (Yinazao, Fantangisña and Asùt Tesoru) were drilled. Most of the material consists of serpentinite mud containing lithic clasts from the underlying forearc crust and mantle as well as from the subducting Pacific Plate. Pelagic sediments and volcanic ash deposits underlying

the mud volcanoes were also recovered. In this study, serpentinite mud samples and ultramafic rocks with various degrees of alteration and serpentinization were investigated in order to provide a detailed characterization of the fluid's composition and transport as well as the tectonic and metamorphic history of the rocks themselves. Accordingly, the following conclusions were obtained:

- Fluid-rock interaction related to basically two different tectonic processes was identified, that is, serpentinization and rodingitization of upper plate forearc mantle fragments incorporated within the subduction channel during burial, carbonation of the already formed serpentinites and formation of secondary serpentine together with other secondary minerals (garnet hematite, magnetite) during their ascent to the seafloor within serpentinite mudflows;
- The formation of serpentine mud is generally localized along fracture zones underneath the serpentine mud seamounts as fault-related fracturing of forearc mantle lithosphere results in an extensive increase of the total rock fragment surface, facilitating the massive reaction of slab-derived fluids with the mantle fragments;
- Several alteration processes are in line with an overall evolution of a subduction-related fluid from c. 350°C (antigorite in serpentinites) to c. 100°C and below (chlorite in rodingite);
- Serpentinization degree increases with proximity to the trench, probably due to enhanced fluid-rock interaction within the shallower parts of the subduction zone;
- The investigated ultramafics show forearc peridotite signature;
- Cpx-bearing harzburgites show depleted signatures, indicating that they are residues after moderate to high degrees of partial melting;
- The serpentinites consist of lizardite and chrysotile as well as brucite and andradite, which constrains an upper temperature limit for the serpentinization processes of 200°–300°C. However, the presence of a fine-grained matrix containing antigorite together with lizardite suggests metamorphic temperatures of at least 340°C;
- Rodingitization took place simultaneously with serpentinization at temperature conditions of at least 228°C as inferred by chlorite geo-thermometry;
- The temperature of carbonation of the already formed serpentinites could be constrained by the presence of Cr-rich garnets, which crystallize below 400°C.

Data Availability Statement

This research used samples provided by the International Ocean Discovery Program (IODP). Information on IODP Expedition 366 data and samples is available at: https://iodp.tamu.edu/scienceops/expeditions/mariana_convergent_margin.html. All data discussed in this contribution are available within the paper as well as in Tables T3 and T4 in Fryer et al. (2017).

Acknowledgments
The structural and petrological studies were carried out within a project funded by the Austrian Science Fund P 31683-N29 to *WK*); the related IODP sample requests are 042192-IODP and 069567IODP. We thank Patty Fryer and Kevin Johnson for their constructive and insightful comments that helped improve the quality of this manuscript. Editorial handling by W. Behr is highly appreciated. The authors are grateful for support from IODP, the JOIDES Resolution Facility, and the scientific staff and crew aboard the JOIDES Resolution during Expedition 366. All authors are extremely grateful to Staff Scientist Trevor Williams for his effort and support before and during IODP Expedition 366, and during postcruise research.

References

Agrinier, P., & Cannat, M. (1997). Oxygen-isotope constraints on serpentinization processes in ultramafic rocks from the mid-Atlantic ridge (23°N). *Proceedings of the Scientific Results*, *153*, 381–388.

Agrinier, P., Hekinian, R., Bideau, D., & Javoy, M. (1995). O and H stable isotope compositions of oceanic crust and upper mantle rocks exposed in the Hess Deep near the Galapagos Triple Junction. *Earth and Planetary Science Letters*, *136*(3–4), 183–196. https://doi.org/10.1016/0012-821X(95)00159-A

Ahmed, A. H. (2013). Highly depleted harzburgite–dunite–chromitite complexes from the Neoproterozoic ophiolite, South Eastern Desert, Egypt, a possible recycled upper mantle lithosphere. *Precambrian Research*, *233*, 173–192. https://doi.org/10.1016/j.precamres.2013.05.001

Allen, D. E., & Seyfried, W. E. J. (2003). Compositional controls on vent fluids from ultramafic-hosted hydrothermal systems at mid-ocean ridges: An experimental study at 400°C, 500 bars. *Geochimica et Cosmochimica Acta*, *67*(8), 1531–1542. https://doi.org/10.1016/S0016-7037(02)01173-0

Anderson, M. O., Chadwick, W., Jr., Hannington, M. D., Merle, S. G., Resing, J. A., Baker, E. T., et al. (2017). Geological interpretation of volcanism and segmentation of the Mariana backarc spreading center between 12.7°N and 18.3°N. *Geochemistry, Geophysics, Geosystems*, *18*(6), 2240–2274. https://doi.org/10.1002/2017GC006813

Andreani, M., Mével, C., Boullier, A. M., & Escartin, J. (2007). Dynamic control on serpentine crystallization in veins: Constraints on hydration processes in oceanic peridotites. *Geochemistry, Geophysics, Geosystems*, *8*(2), Q02012. https://doi.org/10.1029/2006GC001373

Arai, S. (1994). Characterization of spinel peridotites by olivine–spinel compositional relationships: Review and interpretation. *Chemical Geology*, *113*(3–4), 191–204. https://doi.org/10.1016/0009-2541(94)90066-3

Arai, S., Prichard, H. M., Matsumoto, I., & Fisher, P. C. (1999). Platinum-group minerals in podiform chromitite from the Kamuikotan Zone, Hokkaido, Northern Japan. *Resource Geology*, *49*(1), 39–47. https://doi.org/10.1111/j.1751-3928.1999.tb00030.x

Austrheim, H., & Prestvik, T. (2008). Rodingitization and hydration of the oceanic lithosphere as developed in the Leka ophiolite, north-central Norway. *Lithos*, *104*(1–4), 177–198. https://doi.org/10.1016/j.lithos.2007.12.006

Bach, W., Garrido, C. J., Paulick, H., Harvey, J., & Rosner, M. (2004). Seawater-peridotite interactions: First insights from ODP Leg 209, MAR 15°N. *Geochemistry, Geophysics, Geosystems*, *5*(9), Q09F26. https://doi.org/10.1029/2004GC000744

Bach, W., & Klein, F. (2009). The petrology of seafloor rodingites: Insights from geochemical reaction path modeling. *Lithos*, *112*(1–2), 103–117. https://doi.org/10.1016/j.lithos.2008.10.022

Bach, W., Paulick, H., Garrido, C. J., Ildefonse, B., Meurer, W. P., & Humphris, S. E. (2006). Unraveling the sequence of serpentinization reactions: Petrography, mineral chemistry, and petrophysics of serpentinites from MAR 15°N (ODP Leg 209, Site 1274). *Geophysical Research Letters*, *33*(13), L13306. https://doi.org/10.1029/2006GL025681

Baumgartner, R. J., Zaccarini, F., Garuti, G., & Thalhammer, O. A. R. (2013). Mineralogical and geochemical investigation of layered chromitites from the Bracco-Gabbro complex, Ligurian ophiolite, Italy. *Contributions to Mineralogy and Petrology*, *165*(3), 477–493. https://doi.org/10.1007/s00410-012-0818-5

Bevins, R. E., Robinson, D., & Rowbotham, G. (1991). Compositional variations in mafic phyllosilicates from regional low-grade metabasites and application of the chlorite geothermometer. *Journal of Metamorphic Geology*, *9*(6), 711–721. https://doi.org/10.1111/j.1525-1314.1991.tb00560.x

Bideau, D., Hebert, R., Hekinian, R., & Cannat, M. (1991). Metamorphism of deep-seated rocks from the Garrett Ultrafast transform (East Pacific Rise Near 13°25'S). *Journal of Geophysical Research*, *96*(B6), 10079–10099. https://doi.org/10.1029/91JB00243

Bonatti, E., & Michael, P. J. (1989). Mantle peridotites from continental rifts to ocean basins to subduction zones. *Earth and Planetary Science Letters*, *91*(3–4), 297–311. https://doi.org/10.1016/0012-821X(89)90005-8

Bostock, M. G., Hyndman, R. D., Rondenay, S., & Peacock, S. M. (2002). An inverted continental Moho and serpentinization of the forearc mantle. *Nature*, *417*(6888), 536–538. https://doi.org/10.1038/417536a

Bourdelle, F., & Cathelineau, M. (2015). Low-temperature chlorite geothermometry: A graphical representation based on a T–R2+–Si diagram. *European Journal of Mineralogy*, *27*(5), 617–626. https://doi.org/10.1127/ejm/2015/0027-2467

Cannaò, E., Scambelluri, M., Bebout, G. E., Agostini, S., Pettke, T., Godard, M., & Crispini, L. (2020). Ophicarbonate evolution from seafloor to subduction and implications for deep-Earth C cycling. *Chemical Geology*, *546*, 119626. https://doi.org/10.1016/j.chemgeo.2020.119626

Cathelineau, M. (1988). Cation site occupancy in chlorites and illites as a function of temperature. *Clay Minerals*, *23*(4), 471–485. https://doi.org/10.1180/claymin.1988.023.4.13

Cathelineau, M., & Nieva, D. (1985). A chlorite solid solution geothermometer the Los Azufres (Mexico) geothermal system. *Contributions to Mineralogy and Petrology*, *91*(3), 235–244. https://doi.org/10.1007/BF00413350

Chan, L.-H., & Kastner, M. (2000). Lithium isotopic compositions of pore fluids and sediments in the Costa Rica subduction zone: Implications for fluid processes and sediment contribution to the arc volcanoes. *Earth and Planetary Science Letters*, *183*(1–2), 275–290. https://doi.org/10.1016/S0012-821X(00)00275-2

Choi, S. H., Shervais, S. B., & Mukasa, S. B. (2008). Supra-subduction and abyssal mantle peridotites of the coast range ophiolite. *Contributions to Mineralogy and Petrology*, *156*(5), 551–576. https://doi.org/10.1007/s00410-008-0300-6

Clift, P. D., & Lee, J. (1998). Temporal evolution of the Mariana arc during rifting of the Mariana Trough traced through the volcaniclastic record. *The Island Arc*, *7*(3), 496–512. https://doi.org/10.1111/j.1440-1738.1998.00206.x

Coleman, R. G. (1967). Low-temperature reaction zones and alpine ultramafic rocks of California, Oregon, and Washington. *US Geological Survey Bulletin*, *1247*, 1–49. https://doi.org/10.3133/b1247

Collins, N. C., Bebout, G. E., Angiboust, S., Agard, P., Scambelluri, M., Crispini, L., & John, T. (2015). Subduction zone metamorphic pathway for deep carbon cycling: II. Evidence from HP/UHP metabasaltic rocks and ophicarbonates. *Chemical Geology*, *412*, 132–150. https://doi.org/10.1016/j.chemgeo.2015.06.012

Debret, B., Albers, E., Walter, B., Price, R., Barnes, J. D., Beunon, H., et al. (2019). Shallow forearc mantle dynamics and geochemistry: New insights from IODP expedition 366. *Lithos*, *326–327*, 230–245. https://doi.org/10.1016/j.lithos.2018.10.038

De Hoog, J. C. M., Gall, L., & Cornell, D. (2010). Trace element geochemistry of mantle olivine and applications to mantle petrogenesis and geothermobarometry. *Chemical Geology*, *270*(1–4), 196–215. https://doi.org/10.1016/j.chemgeo.2009.11.017

Del Gaudio, A. V., Piller, W. E., Auer, G., Grunert, P., & Kurz, W. (2022). Integrated calcareous nannofossils and planktonic foraminifera biostratigraphy as tool to date serpentinite mud production for Fantangisña seamount on the Mariana forearc (IODP Expedition 366). *Newsletters on Stratigraphy*, *55/3*(3), 255–284. https://doi.org/10.1127/nos/2021/0673

Dick, H. J. B., & Bullen, T. (1984). Chromium spinel as a petrogenetic indicator in Abyssal and Alpine–type peridotites and spatially associated lavas. *Contributions to Mineralogy and Petrology*, *86*(1), 54–76. https://doi.org/10.1007/BF00373711

Dilek, Y., Coulton, A., & Hurst, S. D. (1997). Serpentinization and hydrothermal veining in peridotites at Site 920 in the MARK area. *Proceedings of the Ocean Drilling Program, Scientific Results*, *153*, 35–59.

Epstein, G. S., Bebout, G. E., Angiboust, S., & Agard, P. (2020). Scales of fluid-rock interaction and carbon mobility in the deeply underplated and HP-metamorphosed Schistes Lustrés, Western Alps. *Lithos*, *354–355*, 105229. https://doi.org/10.1016/j.lithos.2019.105229

Evans, B. W. (1977). Metamorphisms of alpine peridotite and serpentinite. *Annual Review of Earth and Planetary Sciences*, *5*(1), 397–447. https://doi.org/10.1146/annurev.ea.05.050177.002145

Evans, B. W. (2004). The serpentinite multisystem revisited: Chrysotile is metastable. *International Geology Review*, *46*(6), 479–506. https://doi.org/10.2747/0020-6814.46.6.479

Frery, E., Fryer, P., Kurz, W., Nguyen, A., Sissmann, O., Uysal, T., & Zhao, J. (2021). Episodicity of structural flow in an active subduction system, new insights from mud volcano's carbonate veins - Scientific ocean drilling expedition IODP 366. *Marine Geology*, *434*, 106431. https://doi.org/10.1016/j.margeo.2021.106431

Frost, B. R. (1975). Contact metamorphism of serpentinite, chloritic blackwall, and rodingite at Paddy-Go-Easy-Pass, Central Cascades,Washington. *Journal of Petrology*, *16*(1), 272–313. https://doi.org/10.1093/petrology/16.1.272

Frost, B. R., & Beard, J. S. (2008). On silica activity and serpentinization: Errata. *Journal of Petrology*, *49*(6), 1253. https://doi.org/10.1093/petrology/egn026

Frost, B. R., Beard, J. S., McCraig, A., & Condliffe, E. (2008). The formation of micro-rodingites from IODP hole U1309D: Key to understanding the process of serpentinization. *Journal of Petrology*, *49*(9), 1579–1588. https://doi.org/10.1093/petrology/egn038

Früh-Green, G. L., Connolly, J. A. D., Plas, A., Kelley, D. S., & Grobety, B. (2004). Serpentinization of oceanic peridotites: Implications for geochemical cycles and biological activity the subseafloor biosphere at mid-ocean ridges. *Geophysical Monograph Series*, *144*, 119–136. https://doi.org/10.1029/144GM08

Früh-Green, G. L., Plas, A., & Lecuyer, C. (1996). Petrologic and stable isotopic constraints on hydrothermal alteration and serpentinization of the EPR shallow mantle at Hess Deep, Site 895. *Proceedings of the Ocean Drilling Program, Scientific Results*, *147*, 109–163.

Fryer, P. (1996). Evolution of the Mariana convergent plate margin system. *Reviews of Geophysics*, *34*(1), 89–125. https://doi.org/10.1029/95RG03476

Fryer, P. (2012). Serpentinite mud volcanism: Observations, processes, and implications. *Annual Review of Marine Science*, *4*(1), 345–373. https://doi.org/10.1146/annurev-marine-120710-100922

Fryer, P. (1992). A synthesis of Leg 125 drilling of serpentine seamounts on the Mariana and Izu-Bonin forearcs. In P. Fryer, J. A. Pearce, L. B. Stokking, et al. (Eds.), *Proceedings of the ocean drilling Program, scientific results* (Vol. 125, pp. 593–614).

Fryer, P., & Fryer, G. J. (1987). Origins of nonvolcanic seamounts in a forearc environment. In B. H. Keating, P. Fryer, R. Batiza, & G. W. Boehlert (Eds.), *Seamounts, Islands, and Atolls, Geophysical monograph* (Vol. 43, pp. 61–69). American Geophysical Union. https://doi.org/10.1029/GM043p0061

Fryer, P., Gharib, J., Ross, K., Savov, I., & Mottl, M. J. (2006). Variability in serpentinite mudflow mechanisms and sources: ODP drilling results on Mariana forearc seamounts. *Geochemistry, Geophysics, Geosystems*, *7*(8), Q08014. https://doi.org/10.1029/2005GC001201

Fryer, P., Lockwood, J. P., Becker, N., Phipps, S., & Todd, C. S. (2000). Significance of serpentine mud volcanism in convergent margins. In Y. Dilek, E. M. Moores, D. Elthon, & A. Nicolas (Eds.), *Ophiolites and oceanic crust: New insights from field studies and the ocean drilling program* (pp. 35–52). Geological Society of America. https://doi.org/10.1130/0-8137-2349-3.35

Fryer, P., & Pearce, J. A. (1992). Introduction to the scientific results of Leg 125. *Proceedings of the Ocean Drilling Program Scientific Results*, *125*, 3–11.

Fryer, P., Saboda, K. L., Johnson, L. E., Mackay, M. E., Moore, G. F., & Stoffers, P. (1990). Conical seamount: SeaMARC II, ALVIN submersible, and seismic-reflection studies. In P. Fryer, J. A. Pearce, L. B. Stokking, et al. (Eds.), *Proceedings ODP, initial reports 125* (pp. 5–14). Ocean Drilling Program.

Fryer, P., Wheat, C., & Mottl, M. (1999). Mariana blueschist mud volcanism: Implications for conditions within the subduction zone. *Geology*, *27*(2), 103–106. https://doi.org/10.1130/0091-7613(1999)027<0103:mbmvif>2.3.co;2

Fryer, P., Wheat, C. G., Williams, T., Albers, E., Bekins, B., Debret, B. P. R., & the Expedition 366 Scientists. (2018). Expedition 366 summary. In P. Fryer, C. G. Wheat, & T. T. Williams (Eds.), *Mariana convergent margin and South Chamorro seamount. Proceedings of the International Ocean Discovery Program* (Vol. 366). International Ocean Discovery Program. https://doi.org/10.14379/iodp.proc.366.101.2018

Fryer, P., Wheat, G., Williams, T., & the Expedition 366 Scientists. (2017). Expedition 366 preliminary report: Mariana convergent margin and South Chamorro seamount. International Ocean Discovery Program. https://doi.org/10.14379/iodp.pr.366.2017

Fryer, P., Wheat, G. C., Williams, T., Kelley, C., Johnson, K., Ryan, J., et al. (2020). Mariana serpentine mud volcanism exhumes subducted seamount materials: Implications for the origin of life. *Philosophical Transactions of the Royal Society, A*, *378*(2165), 20180425. https://doi.org/10.1098/rsta.2018.0425

Fryer, P. B., & Salisbury, M. H. (2006). Leg 195 synthesis: Site 1200—Serpentinite seamounts of the Izu-Bonin/Mariana convergent plate margin (ODP Leg 125 and 195 drilling results). In M. Shinohara, M. H. Salisbury, & C. Richter (Eds.), *Proceedings of the ocean drilling Program, scientific results* (Vol. 195, pp. 1–30). Ocean Drilling Program.

Ganguly, J. (1976). The energetics of natural garnet solid solutions: II. Mixing of the calcium silicate end-members. *Contributions to Mineralogy and Petrology*, *55*(1), 81–90. https://doi.org/10.1007/BF00372756

Ghosh, B., & Morishita, T. (2011). Andradite-uvarovite solid solution from hydrothermally altered podiform chromitite Rutland ophiolite, Andaman, India. *The Canadian Mineralogist*, *49*(2), 573–580. https://doi.org/10.3749/canmin.49.2.573

Godard, M., Lagabrielle, Y., Alard, O., & Harvey, J. (2008). Geochemistry of the highly depleted peridotites drilled at ODP Sites 1272 and 1274 (Fifteen-twenty Fracture Zone, Mid-Atlantic Ridge): Implications for mantle dynamics beneath a slow spreading ridge. *Earth and Planetary Science Letters*, *267*(3–4), 410–425. https://doi.org/10.1016/j.epsl.2007.11.058

Grozeva, N. G., Klein, F., Seewald, J. S., & Sylva, S. P. (2017). Experimental study of carbonate formation in oceanic peridotite. *Geochimica et Cosmochimica Acta*, *199*, 264–286. https://doi.org/10.1016/j.gca.2016.10.052

Hart, S. R., & Zindler, A. (1986). In search of a bulk-Earth composition. *Chemical Geology*, *57*(3–4), 247–267. https://doi.org/10.1016/0009-2541(86)90053-7

Hatzipanagiotou, K., & Tsikouras, B. (2001). Rodingite formation from diorite in the Samothraki ophiolite, NE Aegean, Greece. *Geological Journal*, *36*(2), 93–109. https://doi.org/10.1002/gj.887

Hawthorne, F. C., Oberti, R., Harlow, G. E., Maresch, W. V., Martin, R. F., Schumacher, J. C., & Welch, M. D. (2012). IMA report, nomenclature of the amphibole supergroup. *American Mineralogist*, *97*(11–12), 2031–2048. https://doi.org/10.2138/am.2012.4276

Hébert, R., Adamson, A. C., & Komor, S. C. (1990). Metamorphic petrology of ODP Leg 106/109, Hole 670A, serpentinized peridotites: Serpentinization processes at a slow-spreading ridge environment. *Proceedings of the Ocean Drilling Program, Scientific Results*, *106/109*, 103–116.

Heling, D., & Schwarz, A. (1992). Iowaite in serpentine muds at site 778, 779, 780, and 784: A possible cause for the low chlorinity of pore waters. *Proceedings of the Ocean Drilling Program, Scientific Results*, *125*, 313–323.

Hensen, C., Wallmann, K., Schmidt, M., Ranero, C. R., & Suess, E. (2004). Fluid expulsion related to mud extrusion off Costa Rica - A window to the subducting slab. *Geology*, *32*(3), 201–204. https://doi.org/10.1130/G20119.1

Hey, M. H. (1954). A new review of the chlorites. *Mineralogical Magazine*, *30*(224), 277–292. https://doi.org/10.1180/minmag.1954.030.224.01

Honnorez, J., & Kirst, P. (1975). Petrology of rodingites from the equatorial mid-Atlantic fracture zones and their geotectonic significance. *Contributions to Mineralogy and Petrology*, *49*(3), 233–257. https://doi.org/10.1007/BF00376590

Hostetler, R. B., Coleman, R. G., Mumpton, F. A., & Evans, B. W. (1966). Brucite in Alpine serpentinites. *American Mineralogist*, *51*, 75–98.

Hulme, S. M., Wheat, C. G., Fryer, P., & Mottl, M. J. (2010). Pore water chemistry of the Mariana serpentinite mud volcanoes: A window to the seismogenic zone. *Geochemistry, Geophysics, Geosystems*, *11*(1), Q01X09. https://doi.org/10.1029/2009GC002674

Hussong, D. M., & Uyeda, S. (1982). Tectonic processes and the history of the Mariana arc: A synthesis of the results of Deep Sea Drilling Project Leg 60. In M. Lee & R. Powell (Eds.), *Initial reports of the deep sea drilling project* (Vol. 60, pp. 909–929). Ocean Drilling Program.

Hyndman, R. D., & Peacock, S. M. (2003). Serpentinization of the forearc mantle. *Earth and Planetary Science Letters*, *212*(3–4), 417–432. https://doi.org/10.1016/S0012-821X(03)00263-2

Ichiyama, Y., Tsujimori, T., Fryer, P., Michibayashi, K., Tamura, A., & Morishita, T. (2021). Temporal and spatial mineralogical changes in clasts from Mariana serpentinite mud volcanoes: Cooling of the hot forearc-mantle at subduction initiation. *Lithos*, *384–385*, 105941. https://doi.org/10.1016/j.lithos.2020.105941

Irvine, T. N. (1965). Chrome spinel as a petrogenetic indicator: Part I. Theory. *Canadian Journal of Earth Sciences*, *2*(6), 648–671. https://doi.org/10.1139/e65-046

Ishii, T., Robinson, T., Maekawa, H., & Fiske, R. (1992). Petrological studies of peridotites from diapiric serpentinites seamounts in the Izu-Ogasawara Mariana forearc. Leg 125. *Proceedings of the Ocean Drilling Program, Scientific Results*, *125*, 445–463.

Ishizuka, O., Hickey-Vargas, R., Arculus, R. J., Yogodzinski, G. M., Savov, I. P., Kusano, Y., et al. (2018). Age of Izu-Bonin-Mariana arc basement. *Earth and Planetary Science Letters*, *481*, 80–90. https://doi.org/10.1016/j.epsl.2017.10.023

Jagoutz, E., Palme, H., Baddenhausen, H., Blum, K., Cendales, M., Dreibus, G., et al. (1979). The abundance of major, minor and trace elements in the Earth's mantle as derived from primitive ultramafic nodules. *Proceeding of 10th Lunar Planetary Science Conference. Geochimica et Cosmochimica Acta Supplement*, *10*, 2031–2051.

Jamtveit, B., Ragnarsdottir, K. V., & Wood, B. J. (1995). On the origin of zoned grossular-andradite garnets in hydrothermal systems. *European Journal of Mineralogy*, *7*(6), 1399–1410. https://doi.org/10.1127/ejm/7/6/1399

Janecky, D. R., & Seyfried, W. E., Jr. (1986). Hydrothermal serpentinization of peridotite within the oceanic crust: Experimental investigations of mineralogy and major element chemistry. *Geochimica et Cosmochimica Acta*, *50*(7), 1357–1378. https://doi.org/10.1016/0016-7037(86)90311-X

Johnson, K. T. M., Dick, H. J. B., & Shimizu, N. (1990). Melting in the oceanic upper mantle: An ion microprobe study of diopsides in abyssal peridotites. *Journal of Geophysical Research*, *95*(B3), 2661–2678. https://doi.org/10.1029/JB095iB03p02661

Jowett, E. C. (1991). Fitting iron and magnesium into the hydrothermal chlorite geothermometer. *GAC/MAC/SEG Joint Annual Meeting (Toronto), Program with Abstracts*, *16*, A62.

Kamenetsky, V. S., Crawford, A. J., & Meffre, S. (2001). Factors controlling chemistry of magmatic spinel: An empirical study of associated olivine, Cr-spinel and melt inclusions from primitive rocks. *Journal of Petrology*, *42*(4), 655–671. https://doi.org/10.1093/petrology/42.4.655

Kapsiotis, A. N. (2014). Compositional signatures of SSZ-type peridotites from the northern Vourinos ultra-depleted upper mantle suite NW Greece. *Chemie der Erde-Geochemistry*, *74*(4), 783–801. https://doi.org/10.1016/j.chemer.2014.05.004

Kastner, M., Elderfield, H., Jenkins, W. J., Gieskes, J. M., & Gamo, T. (1993). Geochemical and isotopic evidence for fluid flow in the western Nankai subduction zone, Japan. In I. A. Hill, A. Taira, J. V. Firth, et al. (Eds.), *Proceedings of the ocean drilling Program, scientific results* (Vol. 131, pp. 397–413). Ocean Drilling Program. https://doi.org/10.2973/odp.proc.sr.131.143.1993

Kelemen, P. B., & Manning, C. E. (2015). Reevaluating carbon fluxes in subduction zones, what goes down, mostly comes up. *Proceedings of the National Academy of Sciences of the United States of America*, *112*(30), E3997–E4006. https://doi.org/10.1073/pnas.1507889112

Khalil, A. E. S., & Azer, M. K. (2008). Supra-subduction affinity in the Neoproterozoic serpentinites in the Eastern Desert, Egypt: Evidence from mineral composition. *Journal of African Earth Sciences*, *49*(4–5), 136–152. https://doi.org/10.1016/j.jafrearsci.2007.08.002

Klein, F., & Garrido, C. J. (2011). Thermodynamic constraints on mineral carbonation of serpentinized peridotite. *Lithos*, *126*(3–4), 147–160. https://doi.org/10.1016/j.lithos.2011.07.020

Kobayashi, S., & Kaneda, H. (2010). Rodingite with Ti- and Cr-rich vesuvianite from the Sartuohai chromium deposit, Xinjiang, China. *Journal of Mineralogical and Petrological Sciences*, *105*(3), 112–122. https://doi.org/10.2465/jmps.081224

Korzhinskii, D. S. (1968). The theory of metasomatic zoning. *Mineralium Deposita*, *3*, 222–231. https://doi.org/10.1007/BF00207435

Kurz, W., Micheuz, P., Christeson, G. L., Reagan, M., Shervais, J. W., Kutterolf, S., et al. (2019). Postmagmatic tectonic evolution of the outer Izu-Bonin forearc revealed by sediment basin structure and vein microstructure analysis: Implications for a 15 Ma hiatus between Pacific Plate subduction initiation and forearc extension. *Geochemistry, Geophysics, Geosystems*, *20*(12), 5867–5895. https://doi.org/10.1029/2019GC008329

Lafay, R., Montes-Hernandez, G., Janots, E., Chiriac, R., Findling, N., & Toche, F. (2012). Mineral replacement rate in olivine by chrysotile and brucite under high alkaline conditions. *Journal of Crystal Growth*, *347*(1), 62–72. https://doi.org/10.1016/j.jcrysgro.2012.02.040

Laouar, R., Satouh, A., Salmi-Laouar, S., Abdallah, N., Cottin, J.-Y., Bruguier, O., et al. (2017). Petrological, geochemical and isotopic characteristics of the Collo ultramafic rocks (NE Algeria). *Journal of African Earth Sciences*, *125*, 59–72. https://doi.org/10.1016/j.jafrearsci.2016.10.012

Li, X.-P., Rahn, M., & Bucher, K. (2004). Metamorphic processes in rodingites of the Zermatt-Saas ophiolites. *International Geology Reviews*, *46*(1), 28–51. https://doi.org/10.2747/0020-6814.46.1.28

Li, X.-P., Zhang, L., Wei, C., Ai, Y., & Chen, J. (2007). Petrology of rodingite derived from eclogite in western Tianshan, China. *Journal of Metamorphic Petrology*, *25*(3), 363–382. https://doi.org/10.1111/j.1525-1314.2007.00700.x

Ludwig, K. A., Kelley, D. S., Butterfield, D. A., Nelson, B. K., & Früh-Green, G. L. (2006). Formation and evolution of carbonate chimneys at the lost city hydrothermal field. *Geochimica et Cosmochimica Acta*, *70*(14), 3625–3645. https://doi.org/10.1016/j.gca.2006.04.016

Maekawa, H., Fryer, P., & Ozaki, A. (1995). Incipient blueschist-facies metamorphism in the active subduction zone beneath the Mariana forearc. In B. Taylor & J. Natland (Eds.), *Active margins and marginal basins of the western Pacific* (Vol. 88, pp. 281–290). Geophysical Monograph. https://doi.org/10.1029/GM088p0281

Marsaglia, K., Milliken, K., & Doran, L. (2013). Smear slides of marine mud for IODP core description, Volume I. Part 1: Methodology and atlas of siliciclastic and volcanogenic components. *IODP Technical Note*, *1*.

Marsaglia, K., Milliken, K., Leckie, R. M., Tentori, D., & Doran, L. (2015). IODP smear slide digital reference for sediment analysis of marine mud. Part 2: Methodology and Atlas of biogenic components. *IODP Technical Note*, *2*.

Martin, B., & Fyfe, W. S. (1970). Some experimental and theoretical observations on the kinetics of hydration reactions with particular reference to serpentinization. *Chemical Geology*, *6*, 185–202. https://doi.org/10.1016/0009-2541(70)90018-5

Meeker, G. P., Bern, A. M., Brownfield, I. K., Lowers, H. A., Sutley, S. J., Hoefen, T. M., & Vance, J. S. (2003). The composition and Morphology of Amphiboles from the Rainy Creek complex, Near Libby, Montana. *American Mineralogist*, *88*(11–12), 1955–1969. https://doi.org/10.2138/am-2003-11-1239

Melcher, F., Grum, W., Simon, G., Thalhammer, T. V., & Stumpfl, E. F. (1997). Petrogenesis of the ophiolitic giant chromite deposits of Kempirsai, Kazakhstan: A study of solid and fluid inclusions in chromite. *Journal of Petrology*, *38*(10), 1419–1458. https://doi.org/10.1093/petroj/38.10.1419

Mével, C. (2003). Serpentinization of abyssal peridotites at mid-ocean ridges. *Comptes Rendus Geoscience*, *335*(10–11), 825–852. https://doi.org/10.1016/j.crte.2003.08.006

Mével, C., Cannat, M., Gente, P., Marion, E., Auzende, J. M., & Karson, J. A. (1991). Emplacement of deep crustal and mantle rocks on the west median valley wall of the MARK area (MAR, 23°N). *Tectonophysics*, *190*(1), 31–53. https://doi.org/10.1016/0040-1951(91)90353-T

Mittwede, S. K., & Schandl, A. S. (1992). Rodingites from the Southern Appalachian Piedmont, South Carolina, USA. *European Journal of Mineralogy*, *4*(1), 7–16. https://doi.org/10.1127/ejm/4/1/0007

Molina, J. F., & Poli, S. (2000). Carbonate stability and fluid composition in subducted oceanic crust: An experimental study on H_2O-CO_2-bearing basalts. *Earth and Planetary Science Letters*, *176*(3–4), 295–310. https://doi.org/10.1016/S0012-821X(00)00021-2

Morimoto, N., Fabries, J., Ferguson, A. K., Ginzburg, I. V., Ross, M., Seifert, F. A., et al. (1988). Nomenclature of pyroxenes. *Mineralogical Magazine*, *52*(367), 535–550. https://doi.org/10.1180/minmag.1988.052.367.15

Mottl, M. (1992). Porewaters from serpentinite seamounts in the Mariana and Izu-Bonin forearcs, Leg 125: Evidence for volatiles from the subducting slab. In P. Fryer, J. A. Pearce, L. B. Stokking, et al. (Eds.), *Proceedings ODP, scientific results* (Vol. 125, pp. 373–385). Ocean Drilling Program.

Mottl, M. J., Komor, S. C., Fryer, P., & Moyer, C. L. (2003). Deep-slab fluids fuel extremophilic Archaea on a Mariana forearc serpentinite mud volcano: Ocean Drilling Program Leg 195. *Geochemistry, Geophysics, Geosystems*, *4*(11), 9009. https://doi.org/10.1029/2003GC000588

Mottl, M. J., Wheat, C. G., Fryer, P., Gharib, J., & Martin, J. B. (2004). Chemistry of springs across the Mariana forearc shows progressive devolatilization of the subducting plate. *Geochimica et Cosmochimica Acta*, *68*(23), 4915–4933. https://doi.org/10.1016/j.gca.2004.05.037

Nagaya, T., Walker, A. M., Wookey, J., Wallis, S. R., Ishii, K., & Kendall, J. M. (2016). Seismic evidence for flow in the hydrated mantle wedge of the Ryukyu subduction zone. *Scientific Reports*, *6*(1), 29981. https://doi.org/10.1038/srep29981

Nesbitt, H. W., & Brickner, O. P. (1978). Low temperature alteration processes affecting ultramafic bodies. *Geochimica et Cosmochimica Acta*, *42*(4), 403–409. https://doi.org/10.1016/0016-7037(78)90271-5

Niu, Y., Langmuir, C. H., & Kinzler, R. J. (1997). The origin of abyssal peridotites: A new perspective. *Earth and Planetary Science Letters*, *152*(1–4), 251–265. https://doi.org/10.1016/S0012-821X(97)00119-2

Normand, C., Williams-Jones, A. E., Martin, R. F., & Vali, H. (2002). Hydrothermal alteration of olivine in a flow-through autoclave: Nucleation and growth of serpentine phases. *American Mineralogist*, *87*(11–12), 1699–1709. https://doi.org/10.2138/am-2002-11-1220

O'Hanley, D. S., Schandl, E. S., & Wicks, F. J. (1992). The origin of rodingites from Cassiar, British Columbia, and their use to estimate T and P(H_2O) during serpentinization. *Geochimica et Cosmochimica Acta*, *56*(1), 97–108. https://doi.org/10.1016/0016-7037(92)90119-4

Oakley, A. J. (2008). *A multi-channel seismic and bathymetric investigation of the central Mariana convergent margin, (Doctoral dissertation)*. University of Hawaii. Retrieved from University of Hawaii https://www.soest.hawaii.edu/gg/academics/theses/Oakley%20Dissertation%202008.pdf

Oakley, A. J., Taylor, B., Fryer, P., Moore, G. F., Goodliffe, A. M., & Morgan, J. K. (2007). Emplacement, growth, and gravitational deformation of serpentinite seamounts on the Mariana forearc. *Geophysical Journal International*, *170*(2), 615–634. https://doi.org/10.1111/j.1365-246X.2007.03451.x

Oakley, A. J., Taylor, B., & Moore, G. F. (2008). Pacific plate subduction beneath the central Mariana and Izu-Bonin fore arcs: New insights from an old margin. *Geochemistry, Geophysics, Geosystems*, *9*(6), Q06003. https://doi.org/10.1029/2007GC001820

Oakley, A. J., Taylor, B., Moore, G. F., & Goodliffe, A. (2009). Sedimentary, volcanic, and tectonic processes of the central Mariana Arc: Mariana Trough back-arc basin formation and the West Mariana Ridge. *Geochemistry, Geophysics, Geosystems*, *10*(8), Q08X07. https://doi.org/10.1029/2008GC002312

Oberti, R., Cannillo, E., & Toscani, G. (2012). How to name amphiboles after the IMA2012 report: Rules of thumb and a new PC program for monoclinic amphiboles. *Periodico di Mineralogia*, *81*, 257–267. https://doi.org/10.2451/2012PM0015

O'Brien, J. P., & Rodgers, K. A. (1973). Xonotlite and rodingites from Wairere, New Zealand. *Mineralogical Magazine*, *39*(302), 233–240. https://doi.org/10.1017/minmag.1973.039.302.11

O'Hanley, D. S. (1996). *Serpentinites: Records of tectonic and petrological history. Oxford monographs on geology and geophysics*. Oxford University Press.

O'Hanley, D. S., & Wicks, F. J. (1995). Conditions of formation of lizardite, chrysotile and antigorite, Cassiar, British Columbia. *The Canadian Mineralogist*, *33*, 753–773.

Ortoleva, P., Merino, E., Moore, C., & Chadam, J. (1987). Geochemical self-organisation I: Reaction-transport feedbacks and modelling approach. *American Journal of Science*, *287*(10), 979–1007. https://doi.org/10.2475/ajs.287.10.979

Pabst, S., Zack, T., Savov, I. P., Ludwig, T., Rost, D., Tonarini, S., & Vicenzi, E. P. (2011). The fate of oceanic slabs in the shallow mantle: Insights from boron isotopes and light element composition of metasomatized blueschists from the Mariana forearc. *Lithos*, *132*, 162–179. https://doi.org/10.1016/j.lithos.2011.11.010

Parkinson, I. J., & Pearce, J. A. (1998). Peridotites from the Izu-Bonin-Mariana forearc (ODP Leg 125): Evidence for mantle melting and melt-mantle interaction in a supra-subduction zone setting. *Journal of Petrology*, *39*(9), 1577–1618. https://doi.org/10.1093/petroj/39.9.1577

Paulick, H., Bach, W., Godard, M., Hoog, C.-J., Suhr, G., & Harvey, J. (2006). Geochemistry of abyssal peridotites (Mid-Atlantic Ridge, 15°20′N, ODP Leg 209): Implications for fluid/rock interaction in slow spreading environments. *Chemical Geology*, *234*(3–4), 179–210. https://doi.org/10.1016/j.chemgeo.2006.04.011

Peacock, S. M., van Keken, P. E., Holloway, S. D., Hacker, B. R., Abers, G. A., & Fergason, R. L. (2005). Thermal structure of the Costa Rica–Nicaragua subduction zone. *Physics of the Earth and Planetary Interiors*, *149*(1–2), 187–200. https://doi.org/10.1016/j.pepi.2004.08.030

Peacock, S. M. (1990). Fluid Processes in subduction zones. *Science*, *248*(4953), 329–337. https://doi.org/10.1126/science.248.4953.329

Pearce, J. A., Barker, P. F., Edwards, S. J., Parkinson, I. J., & Leat, P. T. (2000). Geochemistry and tectonic significance of peridotites from the South Sandwich arc-basin system, South Atlantic. *Contributions to Mineralogy and Petrology*, *139*(1), 36–53. https://doi.org/10.1007/s004100050572

Pearce, J. A., Van der Laan, S. R., Arculus, R. J., Murton, B. J., Ishii, T., Peate, D. W., & Parkinson, I. J. (1992). Boninite and Harzburgite from Leg 125 (Bonin-Mariana Forearc): A case study of Magma Genesis during the initial stages of subduction. *Proceedings of the Ocean Drilling Program, Scientific Results*, *125*, 623–659.

Piccoli, F., Vitale, A., Beyssac, O., Martinez, I., Ague, J. J., & Chaduteau, C. (2016). Carbonation by fluid – Rock interactions at high-pressure conditions: Implications for carbon cycling in subduction zones. *Earth and Planetary Science Letters*, *1*, 1–14. https://doi.org/10.1016/j.epsl.2016.03.045

Poli, S., Franzolin, E., Fumagalli, P., & Crottini, A. (2009). The transport of carbon and hydrogen in subducted oceanic crust: An experimental study to 5 GPa. *Earth and Planetary Science Letters*, *278*(3–4), 350–360. https://doi.org/10.1016/j.epsl.2008.12.022

Prichard, H. M. (1979). A petrographic study of the process of serpentinization in ophiolites and the ocean crust. *Contributions to Mineralogy and Petrology*, *68*(3), 231–241. https://doi.org/10.1007/BF00371544

Proenza, J. A., Sole, J., & Melgarejo, J. C. (1999). Uvarovite in podiform chromitite: The Moa-Baracoa ophiolitic massif, Cuba. *The Canadian Mineralogist*, *37*, 679–690.

Putnis, A. (2009). Mineral replacement reactions. *Reviews in Mineralogy and Geochemistry*, *70*(1), 87–124. https://doi.org/10.2138/rmg.2009.70.3

Python, M., Ceuleneer, G., Ishida, Y., Barrat, J.-A., & Arai, S. (2007). Oman diopsidites: A new lithology diagnostic of very high temperature hydrothermal circulation in mantle peridotite below oceanic spreading centres. *Earth and Planetary Science Letters*, *255*(3–4), 289–305. https://doi.org/10.1016/j.epsl.2006.12.030

Reagan, M. K., Heaton, D. E., Schmitz, M. D., Pearce, J. A., Shervais, J. W., & Koppers, A. A. P. (2019). Forearc ages reveal extensive short-lived and rapid seafloor spreading following subduction initiation. *Earth and Planetary Science Letters*, *506*, 520–529. https://doi.org/10.1016/j.epsl.2018.11.020

Reagan, M. K., Pearce, J. A., Petronotis, K., Almeev, R., Avery, A. A., Carvallo, C., et al. (2017). Subduction initiation and ophiolite crust: New insights from IODP drilling. *International Geology Review*, *59*(11), 1439–1450. https://doi.org/10.1080/00206814.2016.1276482

Rupke, L. H., Morgan, J. P., Hort, M., & Connolly, J. (2004). Serpentine and the subduction zone water cycle. *Earth and Planetary Science Letters*, *223*(1–2), 17–34. https://doi.org/10.1016/j.epsl.2004.04.018

Saffer, D. M., & Tobin, H. J. (2011). Hydrogeology and mechanics of subduction zone forearcs: Fluid flow and pore pressure. *Annual Review of Earth and Planetary Sciences*, *39*(1), 157–186. https://doi.org/10.1146/annurev-earth-040610-133408

Sato, H. (1977). Nickel content of basaltic magmas: Identification of primary magmas and a measure of the degree of olivine fractionation. *Lithos*, *10*(2), 112–120. https://doi.org/10.1016/0024-4937(77)90037-8

Sato, T., Mizuno, M., Takata, H., Yamada, T., Isse, T., Mochizuki, K., et al. (2015). Seismic structure and seismicity in the southern Mariana Trough and their relation to hydrothermal activity. In J. Ishibashi, K. Okino, & M. Sunamura (Eds.), *Subseafloor biosphere linked to hydrothermal systems*. Springer. https://doi.org/10.1007/978-4-431-54865-2_18

Scambelluri, M., Bebout, G. E., Belmonte, D., Gilio, M., Campomenosi, N., Collins, N., & Crispini, L. (2016). Carbonation of subduction-zone serpentinite (high-pressure ophicarbonate; Ligurian Western Alps) and implications for the deep carbon cycling. *Earth and Planetary Science Letters*, *441*, 155–166. https://doi.org/10.1016/j.epsl.2016.02.034

Scambelluri, M., Cannaò, E., & Gilio, M. (2019). The water and fluid-mobile element cycles during serpentinite subduction. A review. *European Journal of Mineralogy*, *31*(3), 405–428. https://doi.org/10.1127/ejm/2019/0031-2842

Schandl, E. S., O'Hanley, D. S., & Wicks, F. J. (1989). Rodingites in serpentinized ultramafic rocks of the Abitibi Greenstone belt, Ontario. *The Canadian Mineralogist*, *27*, 579–591.

Schmidt, M. W., & Poli, S. (1998). Experimentally based water budgets for dehydrating slabs and consequences for arc magma generation. *Earth and Planetary Science Letters*, *163*(1–4), 361–379. https://doi.org/10.1016/S0012-821X(98)00142-3

Schmitt, A. C., Tokuda, M., Yoshiasa, A., & Nishiyama, T. (2019). Titanian andradite in the Nomo rodingite: Chemistry, crystallography, and reaction relations. *Journal of Mineralogical and Petrological Sciences*, *114*(3), 111–121. https://doi.org/10.2465/jmps.180731

Schroeder, T., John, B., & Frost, B. R. (2002). Geologic implications of seawater circulation through peridotite exposed at slow-spreading ridges. *Geology*, *30*(4), 367–370. https://doi.org/10.1130/0091-7613(2002)030<0367:giosct>2.0.co;2

Schwartz, S., Guillot, S., Reynard, B., Lafay, R., Debret, B., Nicollet, C., et al. (2013). Pressure–temperature estimates of the lizardite/antigorite transition in high pressure serpentinites. *Lithos*, *178*, 197–210. https://doi.org/10.1016/j.lithos.2012.11.023

Seyfried, W. E., Jr., & Dibble, W. E., Jr. (1980). Sea water–peridotite interaction at 300°C and 500 bars: Implications for the origin of oceanic serpentinites. *Geochimica et Cosmochimica Acta*, *44*(2), 309–321. https://doi.org/10.1016/0016-7037(80)90139-8

Seyfried, W. E., Jr., Foustoukos, D. I., & Fu, Q. (2007). Redox evolution and mass transfer during serpentinization: An experimental and theoretical study at 200°C, 500 bar with implications for ultramafic-hosted hydrothermal systems at mid-ocean ridges. *Geochimica et Cosmochimica Acta*, *71*(15), 3872–3886. https://doi.org/10.1016/j.gca.2007.05.015

Snow, J. E., & Dick, H. J. B. (1995). Pervasive magnesium loss by marine weathering of peridotite. *Geochimica et Cosmochimica Acta*, *59*(20), 4219–4235. https://doi.org/10.1016/0016-7037(95)00239-V

Sobolev, A., & Danyushevsky, L. (1994). Petrology and geochemistry of boninites from the north termination of the Tonga Trench: Constraints on the generation conditions of primary high-Ca boninite magmas. *Journal of Petrology*, *35*(5), 1183–1211. https://doi.org/10.1093/petrology/35.5.1183

Solomon, E. A., Kastner, M., Wheat, C. G., Jannasch, H., Robertson, G., Davis, E. E., & Morris, J. D. (2009). Long-term hydrogeochemical records in the oceanic basement and forearc prism at the Costa Rica subduction zone. *Earth and Planetary Science Letters*, *282*(1–4), 240–251. https://doi.org/10.1016/j.epsl.2009.03.022

Stern, R. J., & Bloomer, S. H. (1992). Subduction zone infancy: Examples from the Eocene Izu-Bonin-Mariana and Jurassic California arcs. *Geological Society of America Bulletin*, *104*(12), 1621–1636. https://doi.org/10.1130/0016-7606(1992)104<1621:szieft>2.3.co;2

Stern, R. J., Fouch, M. J., & Klemperer, S. L. (2003). An overview of the Izu-Bonin-Mariana subduction factory. In J. Eiler (Ed.), *Inside the subduction factory, Geophysical monograph series* (Vol. 138, pp. 175–22). American Geophysical Union. https://doi.org/10.1029/138GM10

Stern, R. J., & Smoot, C. N. (1998). A bathymetric overview of the Mariana forearc. *Island Arc*, *7*(3), 525–540. https://doi.org/10.1111/j.1440-1738.1998.00208.x

Straub, S. M., Woodhead, J. D., & Arculus, R. J. (2010). Temporal evolution of the Mariana Arc: Mantle wedge and subducted slab controls revealed with a tephra perspective. *Journal of Petrology*, *56*(2), 409–439. https://doi.org/10.1093/petrology/egv005

Tamblyn, R., Zack, T., Schmitt, A. K., Hand, M., Kelsey, D., Morrissey, L., et al. (2019). Blueschist from the Mariana forearc records long-lived residence of material in the subduction channel. *Earth and Planetary Science Letters*, *519*, 171–181. https://doi.org/10.1016/j.epsl.2019.05.013

Tamura, A., & Arai, S. (2006). Harzburgite–dunite–orthopyroxenite suite as a record of supra-subduction zone setting for the Oman ophiolite mantle. *Lithos*, *90*(1–2), 43–56. https://doi.org/10.1016/j.lithos.2005.12.012

Taylor, B., & Fujioka, K. (1992). Rifting and the volcanic-tectonic evolution of the Izu-Bonin-Mariana arc. *Proceedings of the Ocean Drilling Program, Scientific Results*, *126*, 627–651.

Tryon, M. D., Wheat, C. G., & Hilton, D. R. (2010). Fluid sources and pathways of the Costa Rica erosional convergent margin. *Geochemistry, Geophysics, Geosystems*, *11*(4), Q04S22. https://doi.org/10.1029/2009GC002818

Üner, T. (2021). Supra-subduction zone mantle peridotites in the Tethyan Ocean (East Anatolian accretionary complex–Eastern Turkey): Petrological evidence for melting and melt-rock interaction. *Mineralogy and Petrology*, *115*(6), 663–685. https://doi.org/10.1007/s00710-021-00760-0

Uysal, I., Ersoy, E. Y., Dilek, Y., Escayola, M., Sarifakioğlu, E., Saka, S., & Hirata, T. (2013). Depletion and refertilization of the Tethyan oceanic upper mantle as revealed by the early Jurassic Refahiye ophiolite, NE Anatolia-Turkey. *Gondwana Research*, *27*(2), 594–611. https://doi.org/10.1016/j.gr.2013.09.008

Uysal, I., Ersoy, E. Y., Karslı, O., Dilek, Y., Sadıklar, M. B., Ottley, C. J., et al. (2012). Coexistence of abyssal and ultra–depleted SSZ type mantle peridotites in a neo–Tethyan ophiolite in SW Turkey, constrains from mineral composition, whole rock geochemistry (major–trace–REE–PGE) and Re–Os isotope systematics. *Lithos*, *132–133*, 50–69. https://doi.org/10.1016/j.lithos.2011.11.009

Wheat, C. G., Fryer, P., Fisher, A. T., Hulme, S., Jannasch, H., Mottl, M. J., & Becker, K. (2008). Borehole observations of fluid flow from South Chamorro Seamount, an active serpentinite mud volcano in the Mariana forearc. *Earth and Planetary Science Letters*, *267*(3-4), 401–409. https://doi.org/10.1016/j.epsl.2007.11.057

Yardley, B. W. D., Rochelle, C. A., Barnicoat, A. C., & Lloyd, G. E. (1991). Oscillatory zoning in metamorphic minerals: An indicator of infiltration metasomatism. *Mineralogical Magazine*, *55*(380), 357–365. https://doi.org/10.1180/minmag.1991.055.380.06

Zhou, M. F., Robinson, P. T., Malpas, J., Edwards, S. J., & Qi, L. (2005). REE and PGE geochemical constraints on the formation of dunites in the Luobusa Ophiolite, southern Tibet. *Journal of Petrology*, *46*(3), 615–639. https://doi.org/10.1093/petrology/egh091